

# *Disaggregation of SMOS soil moisture over West Africa using the Temperature and Vegetation Dryness Index based on SEVIRI land surface parameters*

Article

Accepted Version

Creative Commons: Attribution-Noncommercial-No Derivative Works 4.0

Tagesson, T., Horion, S., Zaldo Fornies, V., Mendiguren Gonzalez, G., Bulgin, C. E. ORCID: <https://orcid.org/0000-0003-4368-7386>, Ghent, D. and Fensholt, R. (2018) Disaggregation of SMOS soil moisture over West Africa using the Temperature and Vegetation Dryness Index based on SEVIRI land surface parameters. *Remote Sensing of Environment*, 206. pp. 424-441. ISSN 0034-4257 doi: 10.1016/j.rse.2017.12.036 Available at <https://centaur.reading.ac.uk/74711/>

It is advisable to refer to the publisher's version if you intend to cite from the work. See [Guidance on citing](#).

To link to this article DOI: <http://dx.doi.org/10.1016/j.rse.2017.12.036>

Publisher: Elsevier

copyright holders. Terms and conditions for use of this material are defined in the [End User Agreement](#).

[www.reading.ac.uk/centaur](http://www.reading.ac.uk/centaur)

## **CentAUR**

Central Archive at the University of Reading

Reading's research outputs online

# Disaggregation of SMOS soil moisture over West Africa using the Temperature and Vegetation Dryness Index based on SEVIRI land surface parameters

T. Tagesson<sup>1,2,\*</sup>, S. Horion<sup>1,\*</sup>, H. Nieto<sup>3</sup>, V. Zaldo Fornies<sup>1</sup>, G. Mendiguren González<sup>4,5</sup>, C. E. Bulgin<sup>6</sup>, D. Ghent<sup>7</sup>, R. Fensholt<sup>1</sup>

<sup>1</sup> Department of Geosciences and Natural Resource Management (IGN), University of Copenhagen, Øster Voldgade 10, DK-1350 Copenhagen, Denmark

<sup>2</sup> Department of Physical Geography and Ecosystem Analysis, Lund University, Sölvegatan 12, SE- 223 62 Lund,

<sup>3</sup> Efficient Use of Water in Agriculture Program, Institut de Recerca i Tecnologia Agroalimentàries (IRTA), Fruitcentre, Parc Científic i Tecnològic Agroalimentari, Lleida 25003, Spain

<sup>4</sup> Department of hydrology, Geological Survey of Denmark and Greenland (GEUS), Øster Voldgade 10, DK-1350 Copenhagen, Denmark

<sup>5</sup> Department of Environmental Engineering, Technical University of Denmark, 2800 Kgs. Lyngby, Denmark

<sup>6</sup> Department of Meteorology, University of Reading, 3 Earley Gate, PO Box 238, Reading, United Kingdom

<sup>7</sup> Space Research Centre, University of Leicester, University Road Leicester, LE1 7RH, United Kingdom

\*These two authors contributed equally to this research.

<sup>+</sup>Corresponding author: e-mail: torbern.tagesson@ign.ku.dk; Tel. +46 704 993936

## Abstract

The overarching objective of this study was to produce a disaggregated SMOS Soil Moisture (SM) product using land surface parameters from a geostationary satellite in a region covering a diverse range of ecosystem types. SEVIRI data at 15 minute temporal resolution were used to derive the Temperature and Vegetation Dryness Index (TVDI) that served as SM proxy within the disaggregation process. West Africa (3 °N 26°W; 28 °N 26°E) was selected as a case study as it presents both an important North-South climate gradient and a diverse range of ecosystem types. The main challenge was to set up a methodology applicable over a large area that overcomes the constraints of SMOS (low spatial resolution) and TVDI (requires similar atmospheric forcing and triangular shape formed when plotting morning rise temperature versus fraction of vegetation cover) in order to produce a 0.05° resolution disaggregated SMOS SM product at the sub-continental scale.

Consistent cloud cover appeared as one of the main constraints for deriving TVDI, especially during the rainy season and in the southern parts of the region and a large adjustment window (105×105 SEVIRI pixels) was therefore deemed necessary. Both the original and the disaggregated SMOS SM products described well the seasonal dynamics observed at six locations of *in situ* observations. However, there was an overestimation in both products for sites in the humid southern regions; most likely caused by the presence of forest. Both TVDI and the associated disaggregated SM product was found to be highly sensitive to algorithm input parameters; especially for conditions of high fraction of vegetation cover. Additionally, seasonal dynamics in TVDI did not follow the seasonal patterns of SM. Still, its spatial heterogeneity was found to be a good proxy for disaggregating SMOS SM data; main river networks and spatial patterns of SM extremes (i.e. droughts and floods) not seen in the original SMOS SM product were revealed in the disaggregated SM product for a test case of July-September 2012. The disaggregation methodology thereby successfully increased the spatial resolution of SMOS SM, with potential application for local drought/flood monitoring of importance for the livelihood of the population of West Africa.

**Keywords:** TVDI; SMOS; disaggregation; downscaling; soil moisture; SEVIRI; sensitivity analysis

## 1. Introduction

Complex interactions of energy exchange are taking place between different components of the Earth system, notably between the atmosphere, hydrosphere and biosphere (Bonan 2008). A better understanding of such interactions is of high societal relevance for improving assessment of carbon and water fluxes as well as for preventing, monitoring and forecasting extreme events. However, it implies the accurate assessment of essential climate variables, such as soil moisture (SM) that is key to determining the water fluxes between the land surface and the atmosphere (Vinukollu et al. 2011).



Since the 1970s, data from Earth Observation (EO) satellite platforms have been used to overcome the limitations of ground sensors thereby providing timely information on the spatial distribution of SM. Soil moisture affects the emission and absorption of electromagnetic radiation in different regions of the spectrum: 1) MicroWave (MW) backscattered or emitted energy from the ground surface, particularly in the low-frequency microwave range, from 1 to 10 GHz, allows the dielectric constant to be related to SM (Schmugge 1978; Stisen et al. 2008); 2) When the soil is wet the energy balance of the surface is controlled by evaporation from the soil surface and vegetation transpiration and lower surface temperatures are expected in wet soils than in drier soils during daytime (Schmugge 1978). This effect can be captured in the Thermal InfraRed (TIR) region of the electromagnetic spectrum. Additionally, if multiple observations of the land surface are acquired at different times throughout the day, diurnal variability in emitted radiation can be related to the soil thermal inertia (a property that describes the resistance of a material to temperature change) (Wang et al. 2006) and consequently serves as a good indicator of evapotranspiration and SM (Minacapilli et al. 2009; Stisen et al. 2008); and 3) in the optical domain (350-2500 nm), an increase of SM produces an overall decrease in albedo (Bach and Mauser 1994) and specific absorption features in the Short-Wave Infrared Region (SWIR) (Sadeghi et al. 2015).

Each of these spectral regions have advantages and disadvantages for mapping SM (Kerr 2007; Moran et al. 2004). Microwave sensors are insensitive to atmospheric disturbances, but they usually require larger pixel sizes than sensors in the optical or thermal infrared domain, due to the lower emitted energy in this region. This is the case for the Soil Moisture and Ocean Salinity (SMOS) (average pixel size 43 km) (Kerr et al. 2012) and the Soil Moisture Active Passive (SMAP) (30km) (Panciera et al. 2014) missions dedicated to monitor SM, rendering such products less suited for spatially explicit studies of the hydrological cycle at the local scale. Unlike MW sensors, optical and TIR sensors are greatly affected by the atmosphere, and allows a higher spatial resolution of

measurements. The Spinning Enhanced Visible and InfraRed Imager (SEVIRI) instrument aboard the geostationary satellite Meteosat Second Generation (MSG) is an optical and TIR sensor centred over Africa that scans the full Earth disk every 15 min. This high temporal resolution is a major advantage since it allows estimates of soil thermal inertia (morning rise temperature; dTS) (Stisen et al. 2008) and it increases the probability of obtaining cloud free observations for areas with frequent cloud cover.

Given the advantages/disadvantages of different EO retrievals, combining high and low spatial resolution data for improving the SM spatial variability has received considerable scientific attention recently (Malb teau et al. 2016; Merlin et al. 2012; Peng et al. 2017; Wang et al. 2016). Methods for disaggregation of SM products can be classified into three major groups: (1) satellite based methods; (2) methods using an array of geoinformation data and (3) model based methods (Peng et al. 2017). Among satellite based methods, an integration of coarse spatial resolution microwave observations with optical/thermal EO retrievals using a downscaling factor is most commonly used (Peng et al. 2017; Wang et al. 2016). One example of an optical/thermal remote sensing metric closely related to SM variability is the Temperature-Vegetation Dryness Index (TVDI) (Sandholt et al. 2002) based on the triangle/trapezoid (hereinafter called triangle) method, since it empirically delimits the triangle formed when plotting the Land Surface Temperature (LST) or dTS versus a Vegetation Index (VI) (Figure 1) (Carlson et al. 1995; Carlson et al. 1990; Moran et al. 1994; Sandholt et al. 2002; Stisen et al. 2008; Sun et al. 2012; Tang and Li 2017). TVDI is most commonly calculated as:

$$TVDI = \frac{LST - LST_{min}}{LST_{max} - LST_{min}} \quad (1)$$

where LST is the LST for a given pixel;  $LST_{min}$  is minimum LST extracted empirically from the lower boundary of the triangle (the wet edge); and  $LST_{max}$  is maximum LST extracted empirically

from the upper boundary of the triangle (the dry edge) for the vegetation index value of the specific pixel (Figure 1) (Sandholt et al. 2002). The dry edge represents dry soils with low evaporation rates causing LST to be at its maximum as a function of the vegetation fraction whereas the wet edge represents wet soils where the evaporation rate occurs near its potential and thus LST is at its minimum and close to the air temperature. Between these two edges, all intermediate conditions can occur, and all SM conditions can consequently be represented within the LST-VI triangle space (Figure 1) (Sandholt et al. 2002).

The triangle approach has been used in several attempts to disaggregate low spatial resolution microwave SM retrievals. At a field site in the north eastern Tibetan plateau, Wang et al. (2016) investigated the applicability of the TVDI for determining a downscaling factor for multiple source microwave based SM data from the European Space Agency (ESA) Climate Change Initiative (CCI) (Dorigo et al. 2012). At the Iberian peninsula, SMOS SM have been disaggregated using the triangle technique with MODerate resolution Imaging Spectroradiometer (MODIS) LST as input data (Piles et al. 2011; Piles et al. 2014), and in an attempt to overcome the issue of frequent cloud cover MSG SEVIRI LST at 15-min temporal resolution was also used (Piles et al. 2016). Another common approach for disaggregation of SMOS SM is to use the DisPATCH (Disaggregation based on Physical And Theoretical scale CHange) model, which combines thermal and optical imagery in a contextual algorithm to derive Soil Evaporative Efficiency (SEE), and then relate SEE to SM through a physically based model (Djamai et al. 2015; Malbêteau et al. 2016; Merlin et al. 2010; Merlin et al. 2012).

Several assumptions and prerequisites need to be taken into account when applying the triangle method: 1) the presence of all SM and vegetation cover conditions are needed within the spatial domain applied (Sandholt et al. 2002; Stisen et al. 2008); 2) the dimensions of the spatial domain have to be large enough to collect a sufficient amount of LST-VI cases to adequately define the

triangle shape (de Tomás et al. 2014); 3) factors like land cover type and topography should be taken into account to ensure the applicability of the method (Hassan et al. 2007); 4) variations in LST must simply reflect variability in SM, which requires other surface properties and atmospheric forcing to be homogeneous; e.g. available energy (net radiation minus ground heat flux), meteorological conditions over the studied area (solar radiation, total column water vapour, air temperature, and wind speed) as well as homogeneous surface roughness to ensure similar conditions affecting the turbulent heat transport (Gillies and Carlson 1995; Moran et al. 1994); and 5) the strong dependence on the endmembers forming the triangular shape implies that a specific TVDI is only comparable with TVDI estimates derived with the same endmember values. As taken together, these preconditions are difficult to fulfil over the entire triangle space (from bare soil to full vegetation cover; from humid to dry conditions), which limit the applicability of the TVDI approach to localized (spatially and temporally) scales (de Tomás et al. 2014; Garcia et al. 2014; Stisen et al. 2008; Tang and Li 2015) as when attempting to cover larger regions there is a high risk of violating these stated preconditions.

Previous studies have used LST directly in the disaggregation process; however combining soil thermal inertia (dTS) based on MSG SEVIRI LST at 15-min temporal resolution with the TVDI approach allows for a more direct estimate of evaporative fraction (Stisen et al. 2008), which can be implemented in the physically based disaggregation methodology behind DisPATCH (Merlin et al. 2012). The overarching objective of this study was to produce a high-resolution disaggregated SMOS SM product for a region covering a diverse range of ecosystem types. We aimed at doing so by disaggregation of low spatial resolution MW data (SMOS) using dTS based on higher spatial and temporal resolution optical data (SEVIRI). We applied the physically based disaggregation methodology behind DisPATCH (Merlin et al. 2012), thereby taking advantage of both types of EO retrievals for SM assessment and accounting for their respective inherent limitations. The main research questions addressed were:

149 How can TVDI derived from SEVIRI based dTS be implemented to resolve the SM spatial  
150 heterogeneity within a SMOS pixel when produced at sub-continental scale over West Africa? What  
151 are the methodological constraints to overcome in order to produce time series of high-resolution  
152 disaggregated SMOS SM product over regions covering a wide spectrum of ecosystem types ranging  
153 from desert to tropical forests?

154 To address these research questions, time series of SMOS SM and time series of LST and Fractional  
155 Vegetation Cover (FVC) from the MSG SEVIRI instrument were acquired for the period 2010-2015.  
156 TVDI was estimated for tile-based adjustment windows on SEVIRI dTS and FVC. The TVDI  
157 estimates were incorporated into a disaggregation methodology to produce high resolution  
158 disaggregated SMOS SM product for West Africa. The sensitivity of TVDI and disaggregated SMOS  
159 SM to the input parameters were quantified. The original and the disaggregated SMOS SM products  
160 were evaluated against *in situ* SM from sites within the International Soil Moisture Network (ISMN).  
161 Finally, the spatial patterns of disaggregated SM products were evaluated for a specific case of  
162 extreme SM conditions (droughts and floods) in the Sahel 2012.

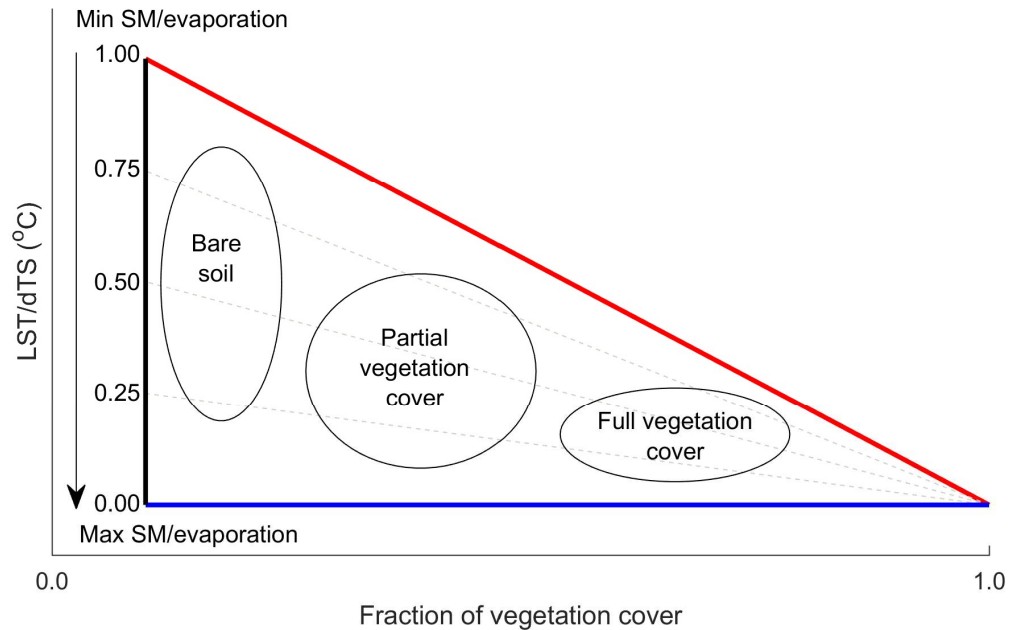


**Figure 1.** Conceptual triangle space with the land surface temperature (LST) or morning rise temperature (dTS) on the y-axis and Fraction of Vegetation Cover (FVC) on the x-axis. The blue line is the wet edge (TVDI=0.00) and the red line is the dry edge (TVDI=1.00). The grey dotted lines are TVDI examples of 0.25, 0.50, and 0.75. The figure is adapted from Peng et al. (2017).

## 2. Materials and Methods

### 2.1. Study area

West Africa was selected as research area for this study (Figure 2) as the climate varies from hot desert in the north to tropical forest climate in the south. The area (3 °N 26°W; 28 °N 26°E) stretches from Senegal in the west to Chad in the east. The climate is controlled by the West African Monsoon and is characterized by a north-south gradient of increasing annual precipitation. The large gradient in precipitation totals is reflected by increasing biomass from north to south as reflected in the fractional vegetation cover (Figure 2). The study area constitutes of  $1.06 \times 10^4$  SMOS pixels and  $5.20 \times 10^5$  SEVIRI pixels.

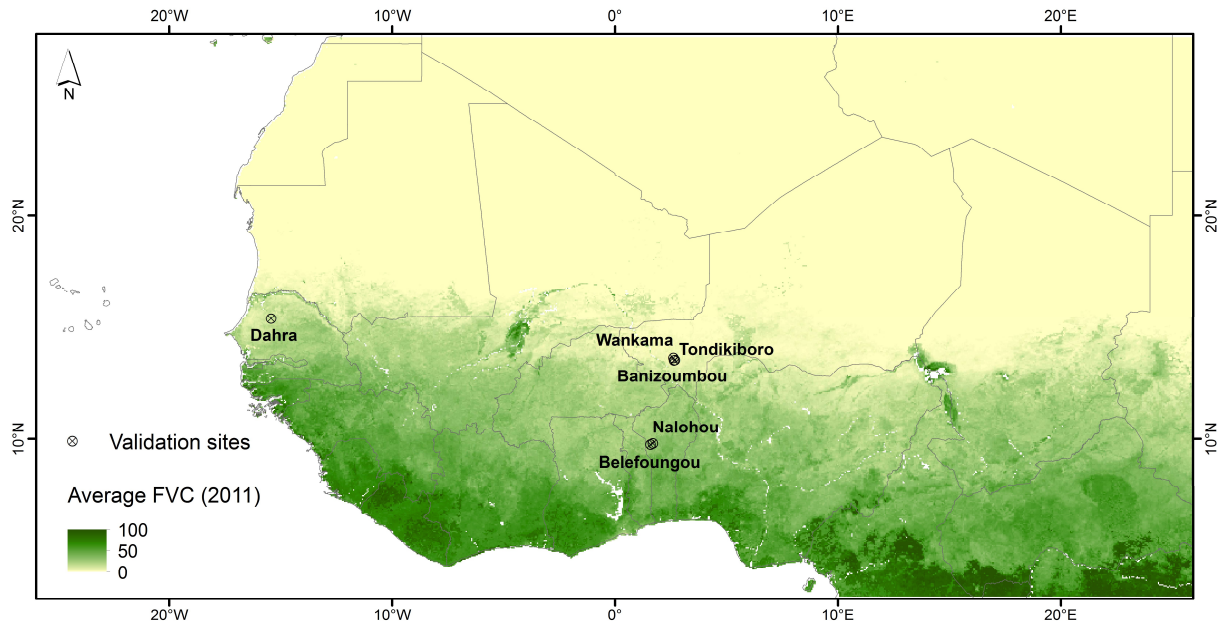


**Figure 2.** Study area with the location of the *in situ* validation sites. The averaged fraction of vegetation cover (FVC) for year 2011 is used as background to illustrate the important north-south gradient in vegetation cover.

## 2.2. Data collection and pre-processing

### 2.2.1 SMOS soil moisture

The SMOS mission includes a passive interferometric radiometer and is the first satellite mission operating at L-band (1.4 GHz). The L-band is less sensitive to green vegetation components and the SMOS multi-angular acquisition capability is additionally used to separate the soil and vegetation signal (Kerr 2007; Wigneron et al. 2007). The SMOS level 2 version-62x SM product was used in this study. We downloaded the SMOS data from 1 June 2010 until 31 December 2015 for the study area. SMOS SM is an average of SM at 0-5 cm depth. The revisiting time at the equator is every 3 days for both ascending and descending passes, which are sun synchronous at 6 am ascending and 6 pm descending. The geolocation accuracy of SMOS is 500 m. The sampling grid of the SMOS data is the Discrete Global Grid (DGG), and it has a node separation of 14.99 km. This is higher than the natural footprint size of SMOS, ranging from 30 to 90 km (average 43km) depending on viewing

angle. Data were reprojected to WGS-84 geographic coordinates using a bilinear resampling method. We used a  $0.35^\circ$  grid ( $\sim 40$  km; which is close to the average natural footprint size of SMOS and is easily dividable with the chosen SEVIRI pixel size) and averaged the SMOS SM estimates of the DGG nodes falling within a  $\pm 0.1^\circ$  area in the centre of each pixel. We only used these central nodes as these are assumably least influenced by neighbouring pixels.

### **2.2.2 Land surface temperature**

Land surface temperatures from SEVIRI from 1 January 2010 to 31 December 2015 were acquired following the procedure described in (Nieto et al. 2011; Rasmussen et al. 2011; Stisen et al. 2007). SEVIRI LST fields are available every 15 minutes for the entire MSG disk centred at  $0^\circ$  longitude and with a native pixel sampling size of 3 km. For consistency with the retrieved FVC data (see below), it was resampled using nearest neighbour to a spatial resolution of  $0.05^\circ$ .

LST was calculated based on SEVIRI channels centered at 10.8 and 12  $\mu\text{m}$ . The European organisation for the exploitation of METeorological SATellites (EUMETSAT) NoWCasting & very short range forecasting Satellite Application Facility (NWC SAF) software (version 2013) was used for converting data to top-of-atmosphere (TOA) brightness temperatures. TOA brightness temperatures were atmospherically corrected for surface emissivity, atmospheric attenuation along the path and emissivity of downward radiation. Spectral emissivity was estimated based on soil and vegetation emissivity endmember values, scaled by the Normalised Difference Vegetation Index (NDVI) and a look-up table (Trigo et al. 2008). SEVIRI NDVI was calculated from daily nadir Bidirectional Reflectance Distribution Function (BRDF)-adjusted reflectance corrected using the Simplified Method for Atmospheric Correction (SMAC) (Proud et al. 2010). The atmospherically corrected brightness temperatures were converted to LST following the generalized split window proposed by Wan and Dozier (1996) for the Advanced Very High Resolution Radiometer (AVHRR)



and MODIS, but adapted to SEVIRI response functions (Jimenez-Munoz and Sobrino 2008; Sobrino and Romaguera 2004). This data process was originally produced for (Nieto et al. 2011; Rasmussen et al. 2011; Stisen et al. 2007), and just applied in this study. For a closer data description we refer to these publications. Furthermore, a quality flag was produced for each LST value based on the cloud mask (PGE01) derived from the NWC SAF software, and quality flags related to clouds, unreliable data, sun-sensor geometry, and when the BRDF inversion failed (Proud et al. 2010; Proud et al. 2014).

### **2.2.3 Fraction of vegetation cover**

Daily FVC derived from SEVIRI and distributed by the Land Surface Analysis Satellite Applications Facility (LSA SAF) were provided by Instituto Português do Mar e Atmosfera (IPMA), in the GLOBTEMP harmonised format (0.05° spatial resolution) for 1 January 2010 to 31 December 2015 (GLOBTEMP 2014; Trigo et al. 2011). The FVC accounts for the amount of vegetation distributed in a horizontal perspective and is therefore an important structural property of a plant canopy, as well as a crucial proxy for studies relying on the partition between soil and vegetation contribution to surface emissivity and temperature. The daily FVC products are based on the  $k_0$  coefficient of a BRDF model for the red (600 nm), near infrared (800nm) and shortwave infrared (1600nm) channels, and is generated using an algorithm that relies on an optimised Spectral Mixture Analysis (SMA) technique (García-Haro et al. 2005). The products also include quality control information that were used to mask out pixels that were not reliable or relevant for this study (i.e. continental water, clouds, snow, unrealistic input ranges, or failure of the algorithm).

### **2.2.4 Surface roughness and atmospheric forcing**

In order to analyse the homogeneity of surface properties and atmospheric forcing in relation to the use of TVDI, we downloaded ERA 5 surface solar radiation downwards (SSRD;  $\text{J m}^{-2}$ ; accumulated at a 3-hour temporal resolution), forecast surface roughness (FSR; m; instantaneous at 12-hour

temporal resolution), total column water vapour (TCWV;  $\text{kg m}^{-2}$ ; instantaneous at 12-hour temporal resolution), wind speed at 100 m height (WS;  $\text{m s}^{-1}$ ; u and v wind components instantaneous at 12-hour temporal resolution), and air temperature at 975hPa level ( $T_{\text{air}}$ ; K; instantaneous at 12-hour temporal resolution)) with a spatial resolution of  $0.1^\circ \times 0.1^\circ$  (interpolated using a bilinear method from  $31 \times 31 \text{ km}$  spatial resolution) from 1 January 2010-31 December 2015 from the European Centre for Medium-Range Weather Forecasts (ECMWF 2017). Collected WS and  $T_{\text{air}}$  represents conditions from above the blending height, since near surface variability in these parameters is driven by local meteorological conditions and is therefore allowed to be heterogeneous at the scale required for the triangular shape to take form. SSRD was converted to  $\text{W m}^{-2}$  and all variables were averaged to daily values.

#### 2.2.5 *In situ* soil moisture

In order to validate the disaggregation methodology we collected available *in situ* measurements of SM from eight sites within ISMN (Figure 2) (ISMN 2016). Available sites in West Africa with data 2010-2015 were from the AMMA-Catch (Niger and Benin sites) and Dahra (Senegal site) network: Banizoumbou (Niger;  $13.53^\circ \text{N } 2.66^\circ \text{E}$ ), Belefoungou-Mid (Benin;  $9.80^\circ \text{N } 1.71^\circ \text{E}$ ), Belefoungou-Top (Benin;  $9.79^\circ \text{N } 1.71^\circ \text{E}$ ), Dahra (Senegal;  $15.40^\circ \text{N } 15.43^\circ \text{E}$ ), Nalohou-Mid (Benin;  $9.75^\circ \text{N } 1.61^\circ \text{E}$ ), Nalohou-Top (Benin;  $9.74^\circ \text{N } 1.61^\circ \text{E}$ ), Tondikiboro (Niger;  $13.55^\circ \text{N } 2.67^\circ \text{E}$ ) and Wankama (Niger;  $13.65^\circ \text{N } 2.63^\circ \text{E}$ ). *In situ* SM was collected using vertical sampling at all these sites to capture the rooting zone soil profile. For the best possible intercomparison with the SMOS SM soil depth (average 0-5 cm), we only used data collected at the shallowest depths (0.05 m depth for all sites but Nalohou-mid, where the shallowest depth was 0.10 m). The two locations of Belefoungou and Nalohou were averaged before the analysis.

The Niger and Senegal sites are located in the Sahel region characterised by a short rainy season between June and October. The Dahra field site and the Niger region receives around 400mm and 500mm of rain, respectively (Louvet et al. 2015; Tagesson et al. 2015). The vegetation of the Niger sites are typical for cultivated areas of the Sahel, whereas the Dahra site is composed of open woody savannah (Louvet et al. 2015; Tagesson et al. 2016). The Benin sites are located further south in the Soudanian climate zone with an annual precipitation of ~1300mm (Louvet et al. 2015). These sites are thereby characterised by significantly denser vegetation, and woody savannah and tropical forest are typical of these sites (Louvet et al. 2015).

The *in situ* SM observations are from low density networks consisting of one or two sites per pixel which introduces an uncertainty in the representativeness of the sites in relation to the validation of the SM products (Peng et al. 2017). However, sensors at these sites were installed specifically for satellite product evaluation, hence the location of the sites were chosen to be representative for the larger area, and they have previously been used for various satellite product assessments. The *in situ* SM measurements are thereby considered representative for the wider area and applicable in a validation of large-scale satellite based SM estimates.

## **2.3. Data analysis**

### **2.3.1. Temperature and Vegetation Dryness Index (TVDI) as soil moisture proxy**

The TVDI was developed by Price (1990) and later improved notably by Sandholt et al. (2002) and Stisen et al. (2008). It has been widely used for assessing SM and evapotranspiration (Garcia et al. 2014; Han et al. 2010; Jiang et al. 2008; Li et al. 2010; Li et al. 2008; Mallick et al. 2009; Patel et al. 2009; Wang et al. 2004). Several methodological refinements were applied in this study as compared to previous approaches to make it applicable for SMOS disaggregation at the sub-continental scale:

(1) The dTS was used as a substitute for LST as it was demonstrated to be a strong proxy for sensible heat fluxes, thereby improving the TVDI estimates as compared to those based on single (hourly or daily) LST (Stisen et al. 2008). The morning rise temperature was calculated as the change (i.e. slope coefficient ( $^{\circ}\text{C h}^{-1}$ )) in LST between sunrise and noon. A median Theil-Sen procedure was applied since it is known to be robust against non-normality, heteroscedasticity, and temporal autocorrelation (Alcaraz-Segura et al. 2010; Hirsch and Slack 1984; Vanbelle and Hughes 1984) and it is suggested for studies of trends based on time series of data (de Beurs and Henebry 2005). Furthermore, it is resistant to outliers and therefore suitable for assessing the rate of change in short or noisy time-series (Eastman et al. 2009). In order to minimise cloud contamination and erroneous data in the dTS and TVDI calculations, we filtered the FVC and LST data based on provided quality flags. We also excluded all dTS pixels using the following criteria: 1) temporal range of daily time-series  $< 4$  hours; 2) sample size used in the fit  $< 5$  cases; 3)  $\text{dTS} > 10^{\circ}\text{C h}^{-1}$  and  $< 0^{\circ}\text{C h}^{-1}$ ; and 4) poor LST vs time fit ( $r < 0.70$ ). Criteria 1 ensured that dTS was not calculated for pixels with clustered unfiltered data (i.e. only available for a short window of time during the day). Criteria 2 was set in order to ensure a sufficient number of observations. Criteria 3 and 4 were set to filter out observations with residual clouds.

(2) We used the algorithm proposed by Tang et al. (2010) to estimate the dry edge ( $\text{LST}_{\text{max}}$  in equation 1) due to its low sensitivity to outliers (cloud residuals). In order to determine the upper edge of the triangle, we divided the dTS-FVC triangular space into bins with a FVC size of 2.5%. Each bin was separated into 5 subintervals and the maximum dTS of each subinterval was extracted. All subinterval maximum dTS  $<$  the average ( $\text{dTS}_{\text{sub\_mean}}$ ) minus one standard deviation ( $\delta$ ) of these 5 subinterval maximum dTS were removed and a new maximum dTS was calculated and used as the maximum for that specific bin. An ordinary least square linear regression was fitted through the remaining maximum dTS values and their corresponding FVC bins and used as the dry edge. These

310 were the main steps in the algorithm; for a closer description we refer to Tang et al. (2010). The  
311 implementation of the algorithm was slightly modified compared to the original Tang et al. (2010)  
312 algorithm in that all bins to the left of the triangular maximum dTS and all dTS lower than wet edge  
313 (see below) were removed before the fitting.

314 (3) The wet edge ( $LST_{min}$  in equation 1) was calculated as the median of the 10<sup>th</sup> percentile dTS of  
315 the points included in the ten 2.5% FVC bins with highest FVC values. The 10<sup>th</sup> percentile was used  
316 instead of absolute minimum as it is less sensitive to outliers and therefore provides a more robust  
317 assessment of the wet edge.

318 (4) The study region was separated into different tiles. The size of the tiles (i.e. the number of SEVIRI  
319 pixels considered to adjust the dTS-FVC triangle for a given SMOS pixel) was set in such way that  
320 it strictly coincided in location and number with a multiple of the SMOS pixel resolution. This  
321 ensured that the information on spatial heterogeneity within a given SMOS pixel will be based on  
322 TVDI estimates that were derived from the same triangle adjustment. In this way, a SMOS pixel  
323 never over-lapped two different TVDI tiles, thereby maximizing the accuracy of the downscaling. A  
324 tile size of 105×105 SEVIRI pixels was selected for the final SMOS disaggregation (see results  
325 section).

326 (5) Furthermore the TVDI values were excluded based on quality of the dry edge fit ( $r > -0.7$ ), dry  
327 edge intercept values  $> 15$  and  $< 0$ , number of bins for estimating the dry edge  $< 5$ , total number of  
328 points in triangle  $< 500$ , FVC range  $< 0.3$ . These filtering criteria excluded entire 105×105 pixels-  
329 tiles. With these criteria we aimed at ensuring the comparability and temporal consistency of the data,  
330 having representative points over a large enough range of FVC (FVC range and number of bins),  
331 excluding TVDI estimates influenced by possible residual clouds (dry edge intercept range and fit),  
332 as well as having enough pixels to calculate the edges of the triangle and removal of those dates in

which the cloud mask reduces the number of good quality pixels available for edge definition (total number of points and dry edge fit).

### **2.3.2. Fulfilment of the preconditions of spatial dimensions and homogeneity**

Surface properties (FSR) and atmospheric forcing (SSRD, TCWV, WS,  $T_{\text{air}}$ ) should be homogenous within the triangular space for the dTS variability to accurately reflect SM variation. To test for homogeneous surface properties and atmospheric forcing within different sized tiles, we ran a three-step procedure. Firstly, FSR, SSRD, TCWV, WS, and  $T_{\text{air}}$  data were filtered based on the criteria described under point 1 in subsection 2.3.1. Secondly, we estimated the dynamic range of daily averages of FSR, SSRD, TCWV, WS, and  $T_{\text{air}}$  by taking the difference between the 95<sup>th</sup> and the 5<sup>th</sup> percentile for different tile sizes covering the Dahra and the Nalohou field sites. These 2 sites were assumed to be representative for the dry and wet parts of the study area, respectively. The 95<sup>th</sup> and the 5<sup>th</sup> percentile were used to avoid influence from outliers. The analysis of data range as a function of tile sizes started from 1×1 SEVIRI pixels with an increment of 1 pixels up until 200×200 SEVIRI pixels. Finally, percentiles (from 1 to the 100<sup>th</sup> in steps of 1) from the full time-series were calculated for each analysed tile size. This was done to analyse the fraction of the time series affected by heterogeneity in FSR, SSRD, TCWV, WS, and  $T_{\text{air}}$  for the different tile sizes tested.

Thereafter, to test the fulfilment of the stated precondition that the spatial dimensions was large enough to capture a sufficient amount of dTS-FVC cases for the triangular shape to take form, we ran the TVDI analysis for the Dahra and the Nalohou field sites using different tile sizes. The analysis started from 5×5 SMOS pixels (35×35 SEVIRI pixels) with an increment of 5 SMOS pixels to 25×25 SMOS pixels (175×175 SEVIRI pixels). The forming of the triangular shape are dependent on a sufficient number of points included in the triangle, the quality of the dry edge (r), and the dynamic

range in FVC. To analyse the effect of tile size we estimated percentiles (from 1 to the 100<sup>th</sup> in steps of 1) of these parameters from the full time-series for each tile size analysed.

### 2.3.3. Gap-filling of TVDI

The calculated time-series of TVDI was gap-filled using two different approaches: (1) the excluded 105×105 SEVIRI pixels-tiles were filled by using the non-filtered tile nearest in time. This secures gap-filling of the tiles excluded based on the TVDI statistics according section 2.3.1 above. (2) Remaining excluded pixels were filled using long-term average calculated as follow:

$$TVDI_{j,t} = \frac{\overline{TVDI_j}}{\langle TVDI \rangle_{105}} \langle TVDI_t \rangle_{105} \quad (2)$$

where  $TVDI_{j,t}$  is the TVDI at pixel (j) in a specific point in time (t) which is needing to be gap-filled;  $\overline{TVDI_j}$  is the TVDI for the pixel (j) averaged for the entire time-series;  $\langle TVDI_t \rangle_{105}$  is the TVDI averaged for the 105×105 pixels-tile for the point in time which needs to be gap-filled; and  $\langle TVDI \rangle_{105}$  is the TVDI averaged for the 105×105 pixels-tile and averaged for the entire time series. This second gap-filling procedure fills pixels that were excluded based on quality flags of the input data (excluded dTS and FVC data).

### 2.3.4. Disaggregation methodology

The SMOS SM was disaggregated following the methodology in Merlin et al. (2012) where spatial heterogeneity in surface SM within the SMOS pixel is linked with a heterogeneity in the soil evaporative efficiency (SEE). Merlin et al. (2012) chose SEE as high resolution data within the disaggregation methodology because of the strong correlation to surface SM (Anderson et al. 2007) and its stability during daytime under clear skies (Crago and Brutsaert 1996). The disaggregation relationship is expressed as:

$$SM_{\text{disaggregated}} = SM_{\text{SMOS}} + \frac{\partial SM_{\text{model}}}{\partial SEE} (SEE_{\text{SEVIRI}} - \langle SEE_{\text{SEVIRI}} \rangle_{\text{SMOS}}) \quad (3)$$

where  $SM_{\text{disaggregated}}$  is the high-resolution SM product disaggregated from the original SMOS data ( $SM_{\text{SMOS}}$ );  $\frac{\partial SM_{\text{model}}}{\partial SEE}$  is the partial derivative of modelled SM on SEE;  $SEE_{\text{SEVIRI}}$  is high-resolution SEE based on SEVIRI input data; and  $\langle SEE_{\text{SEVIRI}} \rangle_{\text{SMOS}}$  is SEE averaged at SMOS scale.

Merlin et al. (2010) tested the accuracy and robustness of the aggregation methodology using different formulations for modelling SEE. They concluded that the formulation of Noilhan and Planton (1989) was the most applicable when conditions for soil properties were unknown:

$$SEE_{\text{model}} = \frac{1}{2} - \frac{1}{2} \cos \left( \pi \times \frac{SM}{SM_p} \right) \quad (4)$$

where  $SEE_{\text{model}}$  is modelled SEE, and  $SM_p$  is a soil parameter in SM unit. In Merlin et al. (2012)  $SM_p$  was estimated by inverting Equation 4 at SMOS resolution:

$$SM_p = \frac{\pi \times SM_{\text{SMOS}}}{\arccos(1 - 2 \langle SEE_{\text{SEVIRI}} \rangle_{\text{SMOS}})} \quad (5)$$

By inverting equation 5, we got a model for estimating SM based on SEE:

$$SM_{\text{model}} = \frac{SM_p}{\pi} \arccos(1 - 2SEE) \quad (6)$$

Then, by taking the partial derivative of SM on SEE in equation 6, we get:

$$\frac{\partial SM_{\text{model}}}{\partial SE} = \frac{2 \left( \frac{SM_p}{\pi} \right)}{\sqrt{1 - (1 - 2SEE)^2}} \quad (7)$$

Merlin et al. (2012) showed a linear relationship between SEE and surface soil temperature using a physically based dual source energy budget model (Kustas and Norman 1999) and a synthetic data set. Given that TVDI was based on soil thermal inertia (dTS), it should be a strong proxy of the non-evaporative fraction, and SEE then equals (1-TVDI). For a description of the mathematical derivation



of equations 5 and 7; we refer to Appendix A. For a mathematical derivation showing that (1-TVDI) equals SEE in the way it is implemented in the DisPATCH methodology, we refer to Appendix B. Finally, equation 7 was inserted into equation 3 and by setting SEE to (1-TVDI), we obtained a disaggregation model directly based on TVDI.

$$SM_{\text{disaggregated}} = SM_{\text{SMOS}} + \frac{2 \left( \frac{SM_{\text{SMOS}}}{\arccos(1-2\langle(1-TVDI)\rangle_{\text{SMOS}})} \right)}{\sqrt{1-(1-2\langle(1-TVDI)\rangle_{\text{SMOS}})^2}} ((1-TVDI) - \langle(1-TVDI)\rangle_{\text{SMOS}}) \quad (8)$$

### 2.3.5. Sensitivity of TVDI and disaggregated SMOS soil moisture to input data

We analysed the sensitivity of TVDI to its input parameters using a synthetic data set with dTS varying from 0 to 10, and FVC varying from 0 to 1.0. TVDI was estimated by setting the wet edge to 0, dry edge intercept to 10, and dry edge slope to 0.1 dTS 0.01FVC<sup>-1</sup>. We changed one input parameter at the time with ±10% of the total range included in the triangle at steps of 0.1% and recalculated TVDI. The input parameters changed included dTS (±1°C), FVC (±0.10), wet edge (±1°C), dry edge intercept (±1°C), and dry edge slope (±0.1°C 0.01FVC<sup>-1</sup>). The sensitivity of TVDI to the parameters was quantified by fitting an ordinary least square linear regression between recalculated TVDI and % error for each dTS-FVC combination.

To quantify the sensitivity of disaggregated SMOS SM to errors in TVDI, we disaggregated SMOS SM using equation 8 with SMOS SM varying from 0 to 100%, TVDI varying from 0.0 to 1.0, and mean TVDI for each SMOS pixel ( $\langle(TVDI)\rangle_{\text{SMOS}}$ ) set to 0.25, 0.50 and 0.75. We changed TVDI with ±0.1 at steps of 0.01 and repeated the disaggregation procedure. The sensitivity of disaggregated SMOS SM to errors in TVDI was quantified by fitting an ordinary least square linear regression between disaggregated SMOS SM and the TVDI error for each SMOS SM, TVDI, and ( $\langle(TVDI)\rangle_{\text{SMOS}}$ ) combination.

### 2.3.6. Evaluation of soil moisture products

We evaluated both the original and the disaggregated SMOS SM using the *in situ* based SM data sets from ISMN as independent data. The agreements between SMOS based SM and the *in situ* SM were quantified as the root mean square error (RMSE), the product-*in situ* ratio, and by goodness-of-fit when an ordinary least-square linear regression was fitted between SMOS based SM and daily *in situ* SM estimates. Spatial patterns of the disaggregated SMOS SM over West Africa were also evaluated for a specific case of extreme SM conditions (i.e. drought and flood). Monthly anomalies of SM were estimated by subtracting the 2010-2015 climatology from the monthly average SM. July to September (JAS) 2012 was selected as test case because both heavy rainfall events and dry conditions corresponding to the ending of the long-lasting drought of 2011-2012 were registered during that period (de Robert 2012; FEWSNET 2012a, b). Beside JAS also corresponds to growing season months in most West Africa, which makes it an interesting case for evaluating potential monitoring products of hydrological extremes from a food security and disaster management point of view.

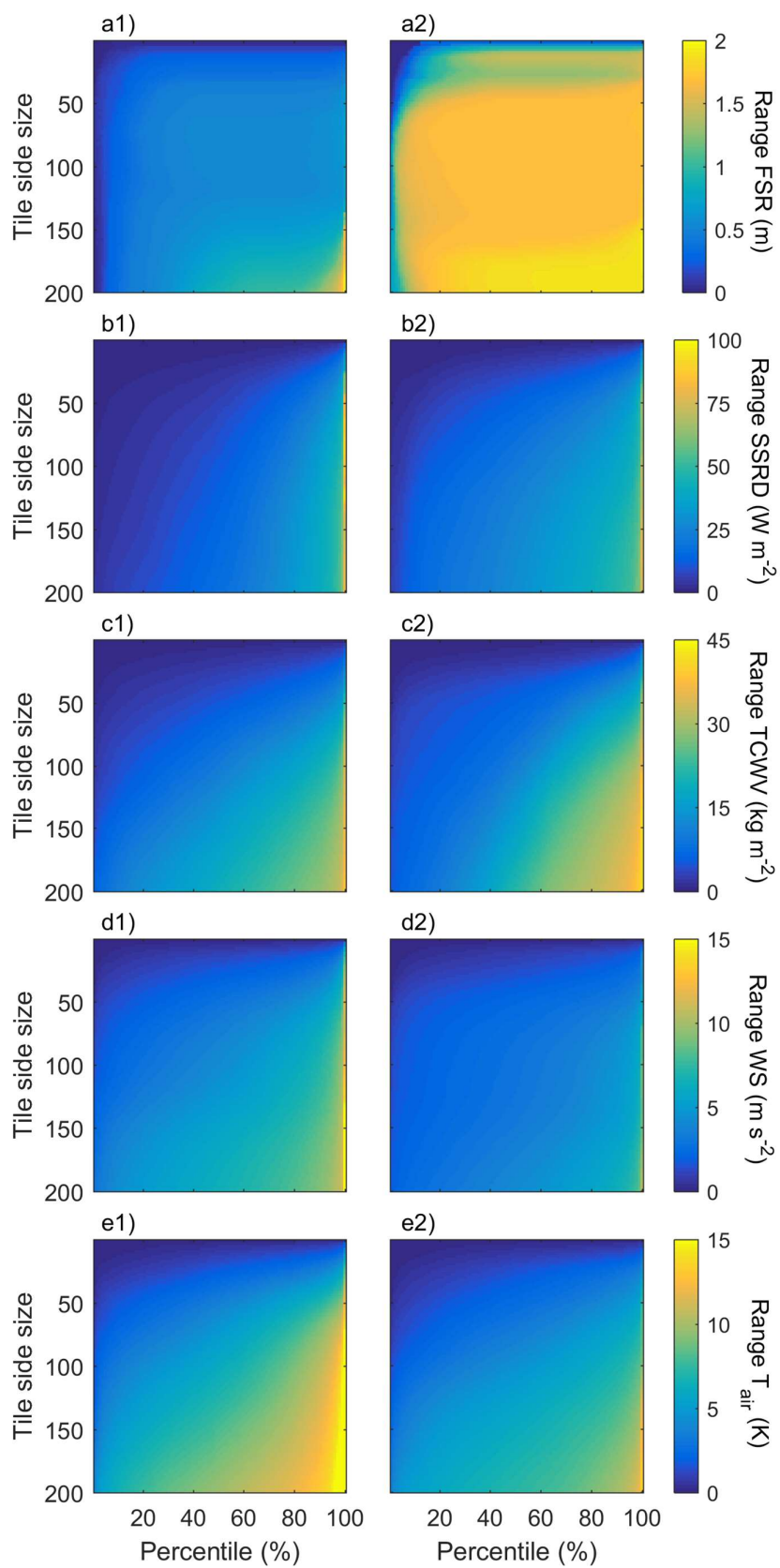
### 3. Results

#### 3.1 Tile size selection and spatio-temporal variability of TVDI

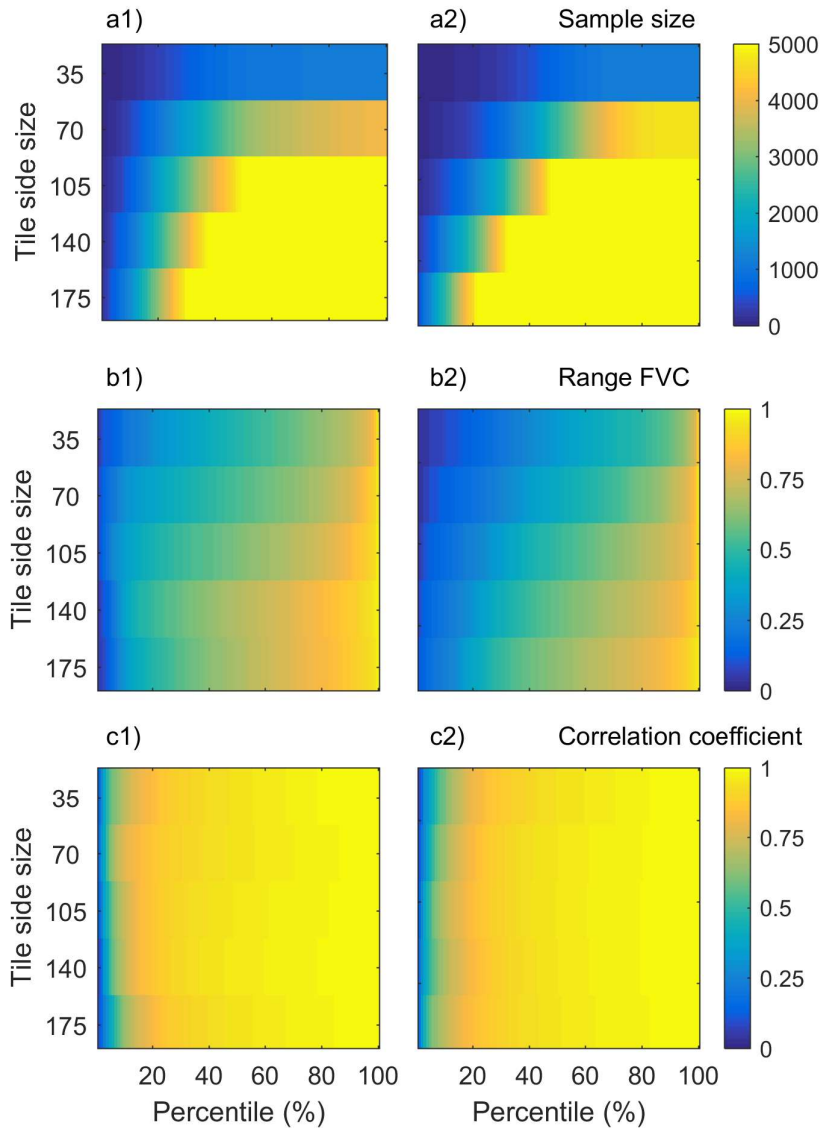
The dynamic range of the parameters affecting available energy within the triangular space differs slightly in their relation to tile size. The dynamic range in FSR was relatively stable over a large spectrum of tile sizes. It was found to increase rapidly to a value close to the maximum where after it remained stable (at  $\sim 0.5$  and  $\sim 1.6$  m for Dahra and Nalohou, respectively) up to a tile size of  $\sim 160 \times 160$  SEVIRI pixels (Figure 3 a). The dynamic range in SSRD, TCWV, WS and  $T_{\text{air}}$  increased more continuously with tile size (Figure 3b and 3c). Up until a tile size of  $100 \times 100$  SEVIRI pixels, daily averaged SSRD was  $< 30 \text{ W m}^{-2}$  for  $\sim 85\%$  and  $\sim 75\%$  of the time series, and daily averaged WS was  $< 6 \text{ m s}^{-1}$  for  $\sim 80\%$  and  $\sim 98\%$  of the time series for Dahra and Nalohou, respectively, (Figure 3 b

and 3d). Total column water vapour (TCWV) and  $T_{\text{air}}$  were more strongly affected by tile size with a larger fraction of the time series having a large dynamic range (Figure 3c and 3e).

Both the sample size and the FVC range increased strongly with tile size (Figure 4). Using the defined filtering criteria for the sample size ( $>500$ ) it can be seen that 40%, 22%, 11%, 4%, and 1% of the time series for Nalohou and 26%, 12%, 8%, 5%, and 3% of the time series for Dahra would be rejected for the different tested tile sizes (with increased tile size order). Tile size is thereby a trade-off between having a large enough sample size allowing for a sufficient amount of dTS-FVC cases, but keeping it as small as possible not to induce uncertainty caused by heterogeneity in the available energy within the triangular space. Reaching a sufficient number of points was challenging during the rainy season, especially in the Southern parts of the study area due to the low number of eligible dTS/FVC pixels (e.g. cloud-free data and good dTS fits) (Figure 5a). As a compromise, when enlarging the tile size to 105 x 105 SEVIRI pixels, more pixels passed the filtering criteria (Figure 5c), and this tile size was chosen for the final analysis.

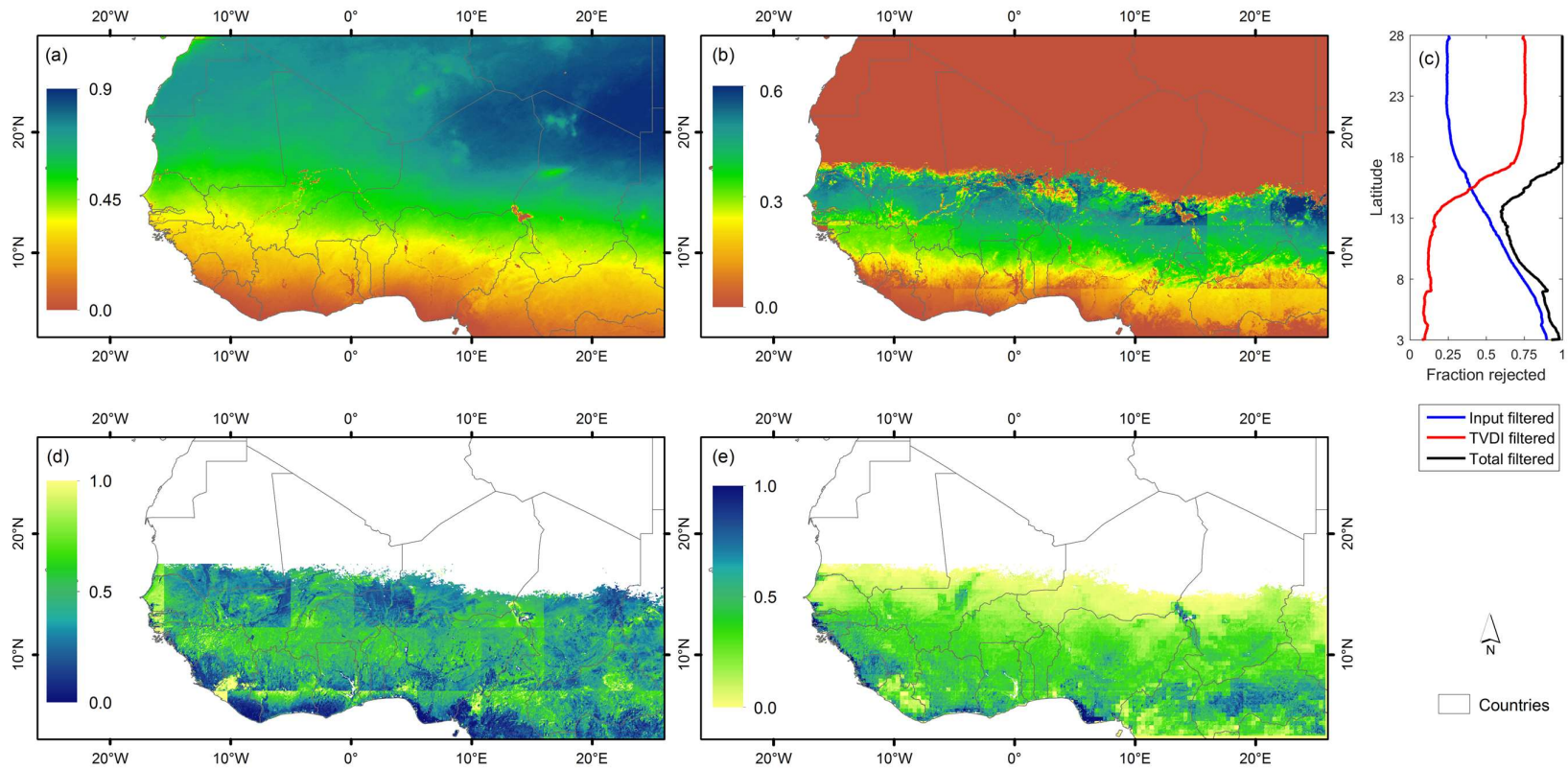


**Figure 3.** Dynamic range in surface properties and atmospheric forcing influencing the homogeneity of available energy within the triangular space. Influence of tile size (y-axis) on the percentiles of the time series (x-axis) of the dynamic range in daily averaged a) forecast surface roughness (FSR) (m); b), surface solar radiation downwards (SSRD) ( $\text{W m}^{-2}$ ); c) total column water vapour (TCWV) ( $\text{kg m}^{-2}$ ); d) wind speed at 100 m height (WS) ( $\text{m s}^{-1}$ ); and e) air temperature at the 975 hPa level ( $T_{\text{air}}$ ) (K) for 1) the Dahra and 2) the Nalohou field sites. The percentiles on the x-axis gives an indication of the fraction of the time series for a given tile size having a dynamic range smaller than the value shown by the colour. For the z-axis, dark blue indicates high homogeneity (i.e. small dynamic range) in surface properties or atmospheric forcing, whereas yellow indicates low homogeneity.



**Figure 4.** Influence of tile size (y-axis) on the percentiles of the time series (x-axis) of the parameters influencing the triangular shape. a) Number of points including in the triangle (N); b) range in fraction of vegetation cover (FVC); and c) correlation coefficient of the dry edge slope (r) for 1) the Dahra and, 2) the Nalohou field sites. The percentiles on the x-axis gives an indication of the fraction of the time-series for a given tile size having a range smaller than the value shown by the colour.

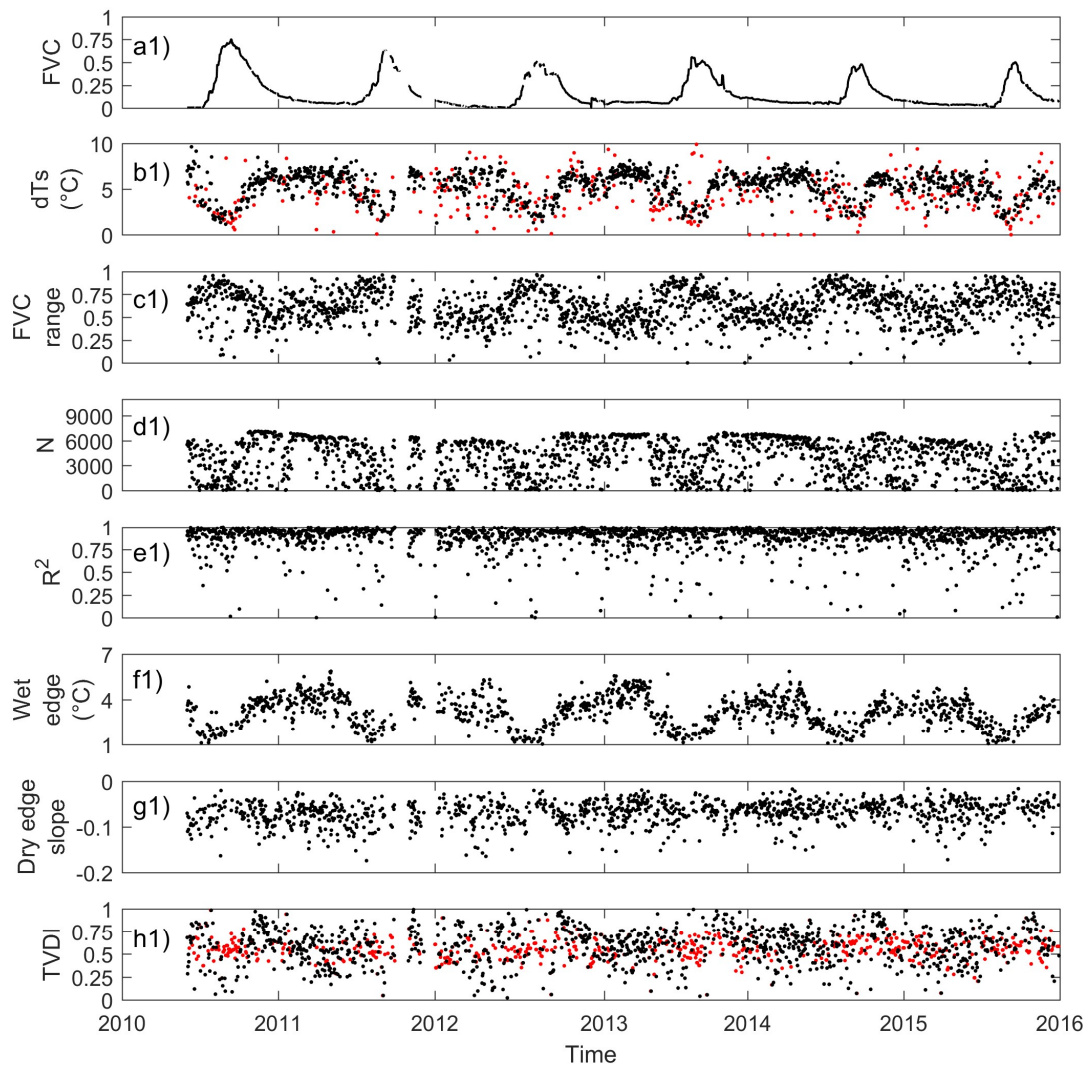
It can be seen that the amount of unfiltered input data (dTS and FVC) increased substantially with latitude (Figure 5a); the further south the higher the fraction of cloud cover and an almost linear loss of data is observed southwards from 20°N (Figure 5c). The amount of data excluded based on TVDI tile statistics had the opposite pattern; at the border between the Sahel and the Sahara the FVC range required for the triangular shape to take form starts to be too low (around 15°N) and above 17.5°N no TVDI retrievals are obtained (Figure 5c). As a result, the largest amount of eligible data for calculating TVDI was observed in the central part of the study area at ~13.5°N. In the spatial pattern of the average TVDI for the entire study period, clear borders between the different tiles can be seen (Figure 5d). However, when combining TVDI with SMOS SM using the disaggregation methodology, the blocky structure disappears and SM heterogeneity across the study area is revealed (Figure 5e; cf subsection 3.3 below).



**Figure 5.** (a) Fraction of data coverage for the input data (dTS and FVC) used in the TVDI calculations; (b) fraction of data coverage for the TVDI calculations when TVDI was filtered based on both TVDI tile statistics and quality flags in input data. (c) Average data exclusion fraction depending on latitude; blue is the fraction of rejected input data, red is the fraction rejected in relation to the TVDI calculation, and black is the total rejected fraction. Included are also: (d) average TVDI for the entire study period; and (e) disaggregated SMOS SM averaged for the entire study period.

490 Clear seasonality was observed in the FVC and dTS time series for the pixels covering the Dahra and  
491 the Nalohou field sites (Figure 6a,b,) whereas TVDI did not exhibit any sign of seasonal patterns and  
492 had a relatively large variability (Figure 6h). The FVC range observed in the adjustment window  
493 varied a lot throughout the year at the semi-arid Sahelian site; even though no clear seasonality was  
494 detected (Figure 6c1). For the southern humid Soudanian savanna site, FVC was also highly variable,  
495 but with a clear seasonality decreasing the FVC range during the rainy season (Figure 6c2). This was  
496 most likely caused by an increased vegetation cover throughout the tile during this part of the  
497 year. The coefficient of determination ( $R^2$ ) of the dry edge fit remained high the entire year ( $> 0.75$ ),  
498 but a larger variability was observed during the rainy season (Figure 6e).





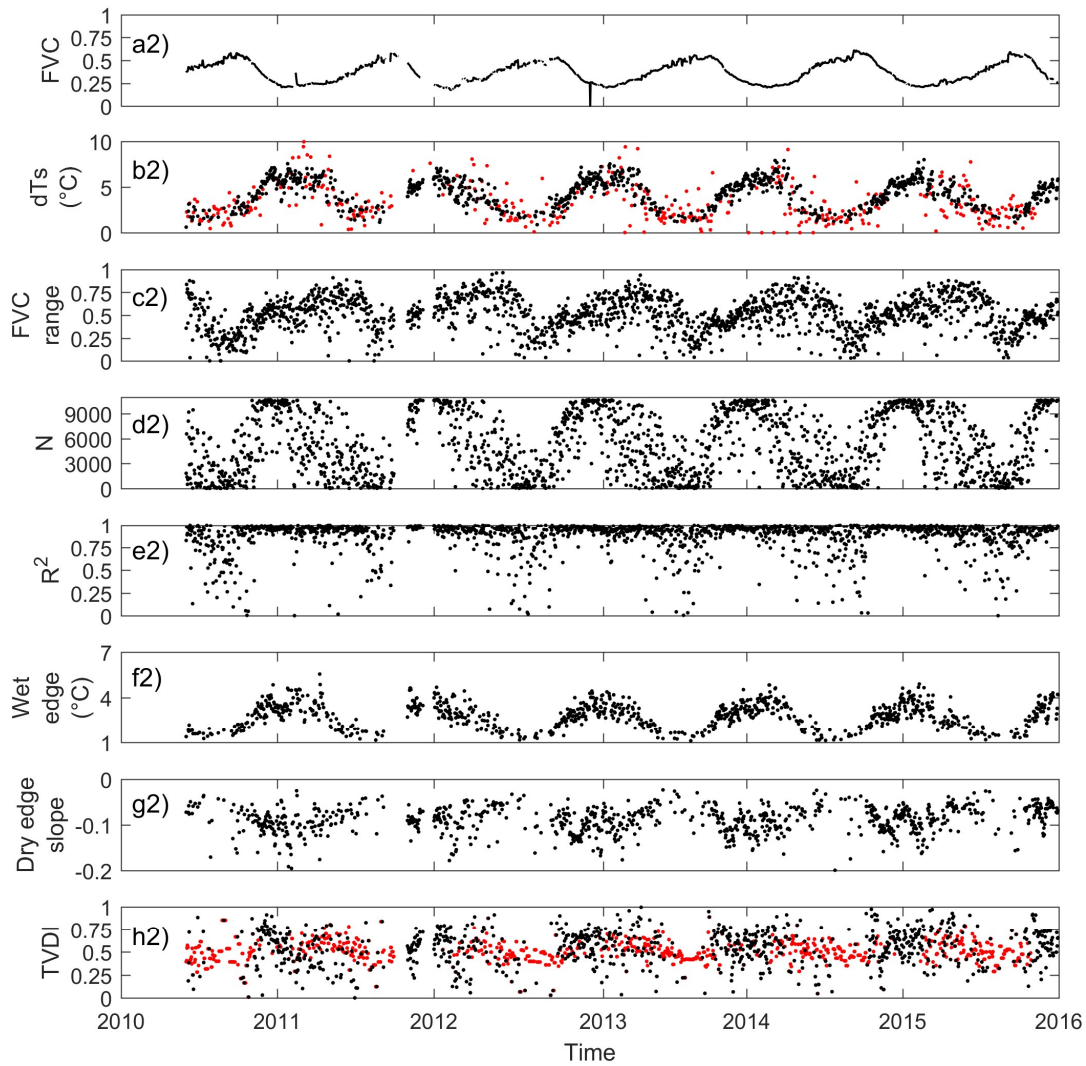
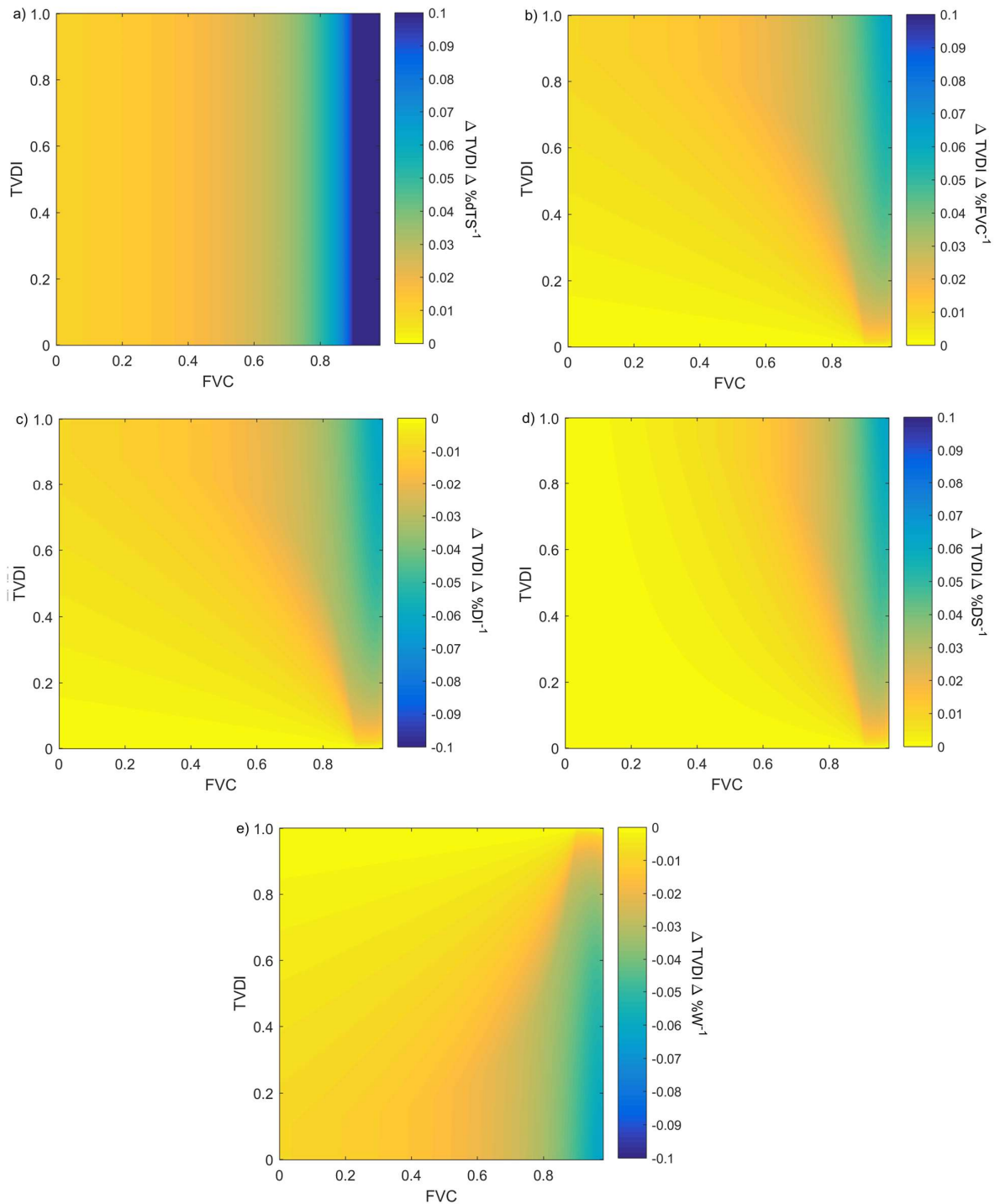


**Figure 6.** Time series of the input parameters, extracts from the TVDI calculation tiles, and final TVDI estimates for (1) Dahra and (2) Nalohou: (a,) fraction of vegetation cover (FVC); (b) unfiltered (red) and filtered (black) morning rise temperature (dTS); (c) range of FVC in the TVDI tiles; (d) total number of points included in the triangle (N); (e) coefficient of determination ( $R^2$ ) for the dry edge fit; (f) wet edge; and (g) dry edge slope. Included are also (h) filtered (black) and gap-filled (red) TVDI estimates (black).

### 3.2. Sensitivity of TVDI and soil moisture to input parameters

The sensitivity analysis of TVDI indicated that sensitivity is strongly dependent on the pixel location within the triangular space. Errors in the input parameters have a very strong impact on the estimated TVDI at the peak of the triangle (upper part of the FVC range) whereas TVDI is less affected close to the vertical catheter of the triangle (lower part of the FVC range) (Figure 7). The reason for this is the small dTS range at the peak of the triangle, resulting in a large sensitivity. An error in the input dTS data have the same impact throughout the entire TVDI range (Figure 7a). As expected, TVDI values close to the dry edge (TVDI=1.0) are more sensitive to errors in the FVC, the dry edge slope and the dry edge intercept (Figure 7b-d) than TVDI values close to the wet edge (Figure 7e). The opposite is the case close to the wet edge (TVDI=0.0) where TVDI values are insensitive to errors in the above mentioned parameters (FVC, the dry edge slope and intercept) but more sensitive to an error in the wet edge.

For low SMOS SM values, disaggregated SM remain low throughout the entire TVDI range (Figure 8 a1-c1) and the disaggregation procedure is thereby rather insensitive to errors in TVDI for this SMOS SM region (Figure 8 a2-c2). However, as SMOS SM increases the range in disaggregated SM start to range from 0-100% (Figure 8 a1-c1), with implications for the sensitivity of the disaggregation procedure. The effect of a change in TVDI is strongest for combinations of low SMOS SM and low TVDI and high SMOS SM and high TVDI (seen in the colour change of Figure 8 a1- c1). For example, when  $\langle(TVDI)\rangle_{SMOS}$  is set to 0.75 disaggregated SM goes from 0 to 100%Vol with a TVDI change from 1.0 to 0.8 (Figure 8c1). This pattern is also visible in the sensitivity of disaggregated SMOS SM to TVDI (Figure 8c2). The most sensitive parts of the triangular space for the disaggregation procedure are thereby close to the wet and dry edges where TVDI approaches 0.0 and 1.0, respectively.



534

535 **Figure 7.** Sensitivity of TVDI to input data and equation parameters: a) morning rise temperature  
 536 (dTS; °C); b) fraction of vegetation cover (FVC); c) dry edge intercept (DI); d) dry edge slope (DS);  
 537 and e) wet edge (W). The % for the temperatures (dTS, DI, and W) and the FVC is a % change in

relation to the range of the triangle. During the analysis we changed one parameter at the time and the rest remained stable.

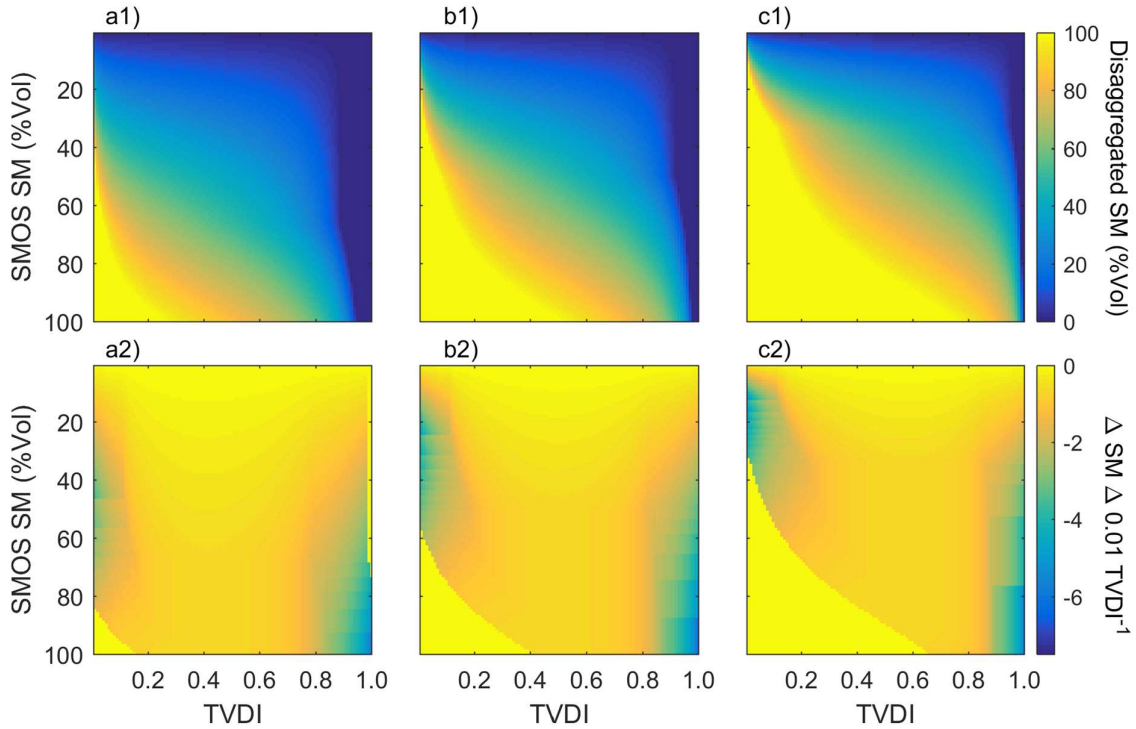
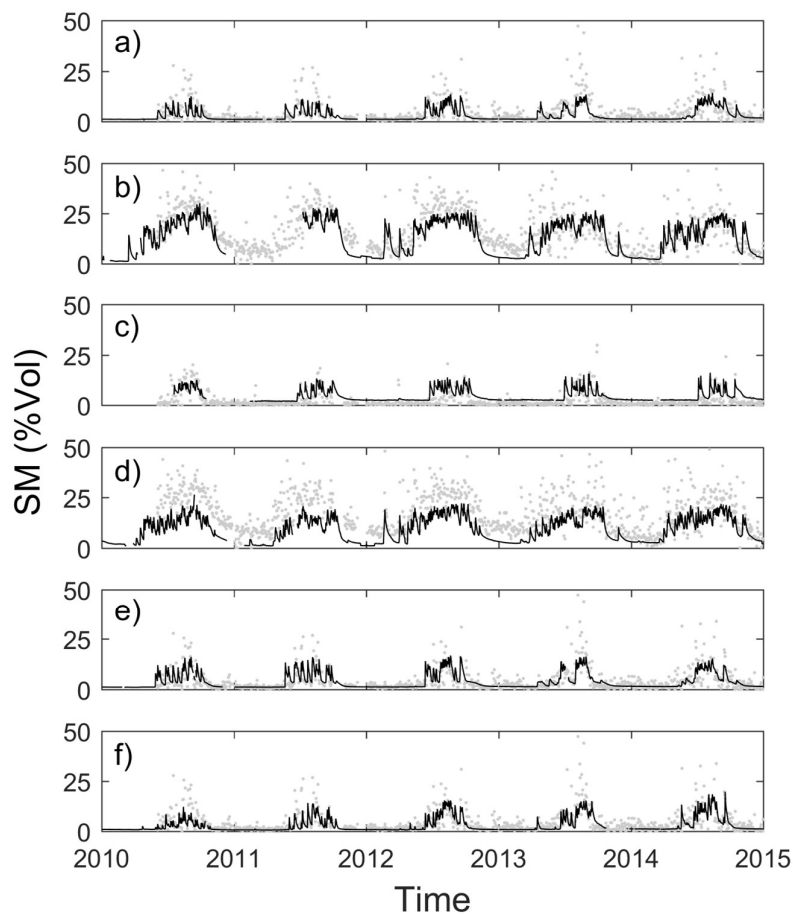


**Figure 8.** Sensitivity of disaggregated SMOS soil moisture (SM; %Vol) to changes in TVDI. Average TVDI in equation 8 was set to a) 0.25, b) 0.50 and c) 0.75. First row (1) shows the actual disaggregated SM for each original SMOS SM -TVDI case and second row (2) shows the changes in disaggregated SM for each 0.01 error in TVDI for each SM -TVDI case.

### 3.3. Evaluation of the SMOS soil moisture products

The original SM product from SMOS generally describes the seasonal dynamics well for the 6 sites (Figure 9). The SMOS SM were on average 8.41%Vol whereas *in situ* SM was on average 6.33%Vol and it can be seen that SMOS SM is overestimated at some of the sites (Belefoungou and Nalohou). This overestimation generated a relatively high RMSE (6.26%Vol) between SMOS SM and *in situ* SM (Table 1). The sites with the highest overestimation are located in the southern humid parts of the study area (Figure 9). The linear function fitted between SMOS SM and *in situ* SM also indicated a

554 general overestimation by SMOS, but high SMOS SM has an even higher overestimation (Figure 10;  
 555 Table 1; slope: 1.26; intercept: 0.77;  $R^2$ : 0.73).



556

557

558 **Figure 9.** Time series of *in situ* measured soil moisture (SM (%Vol)) (thin black line) and Soil  
 559 moisture and Ocean Salinity (SMOS) SM (grey dots) for: a) Banizoumbou; b) Belefoungou; c) Dahra;  
 560 d) Nalohou e) Tondikiboro; and f) Wankama. The location of the different sites is shown in Figure 2.

561

562

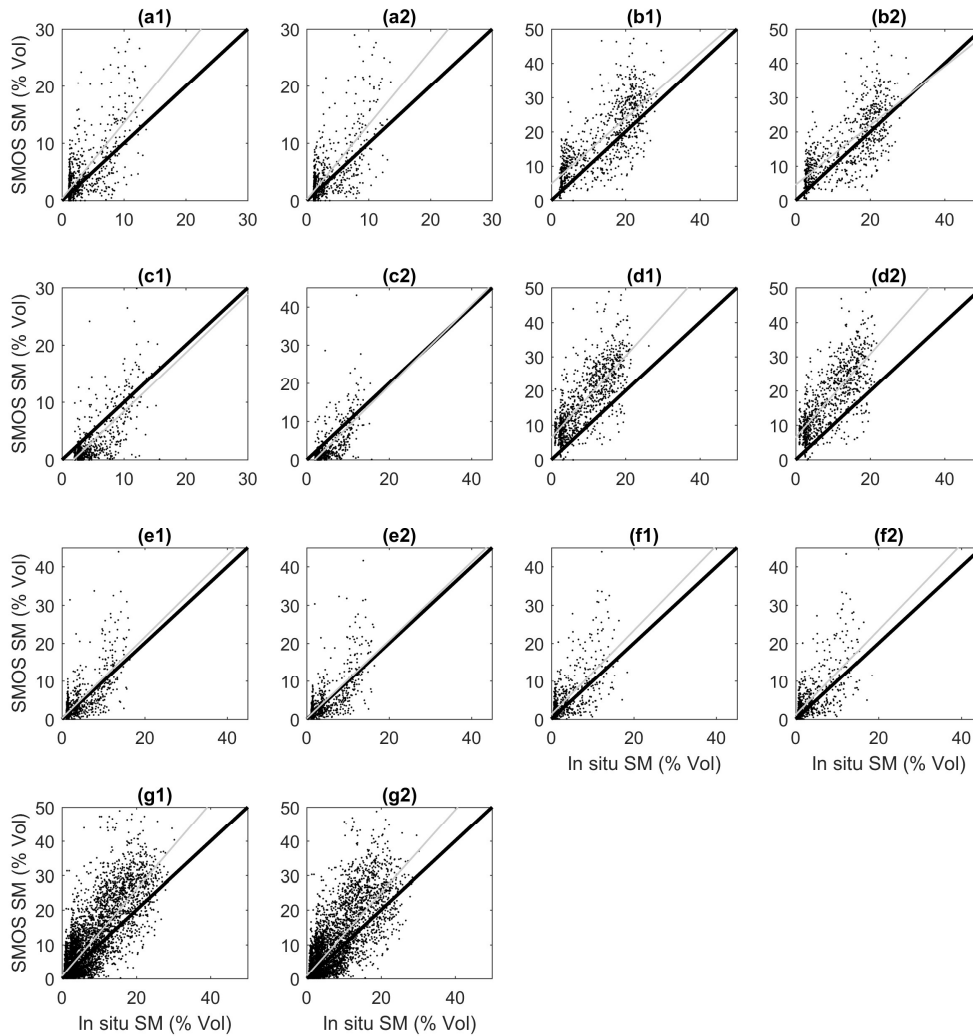


**Figure 10.** Relationship between *in situ* and both original (1) and disaggregated (2) Soil Moisture and Ocean Salinity (SMOS) soil moisture (SM; %Vol) for the pixels used in the evaluation of the disaggregation methodology. The subplots are: a) Banizoumbou; b) Belefoungou; c) Dahra; d) Nalohou; e) Tondikiboro; f) Wankama; and g) all sites combined. The grey line is the ordinary least square linear regression and the black line is the one-to-one ratio. Statistics of the slopes are given in Table 1. The location of the sites can be seen in figure 2.

572

573 **Table 1.** Comparative statistics for the *in situ* validation of the original SMOS and disaggregated SMOS soil moisture. The ratio was the  
 574 product-*in-situ* ratio and it was calculated as original and disaggregated SMOS SM divided by the *in situ* measurements. The analysis was  
 575 conducted for individual sites and with all data combined.

Validation site	Original SMOS						Disaggregated SMOS					
	Slope	Intercept (%Vol)	R2	Mean bias (%Vol)	Ratio	RMSE (%Vol)	Slope	Intercept (%Vol)	R2	Mean bias (%Vol)	Ratio	RMSE (%Vol)
Banizoumbou (BAN)	1.32	0.35	0.58	-1.36	1.44	4.45	1.30	0.19	0.59	-1.13	1.36	4.18
Belefourou (BEL)	0.95	4.87	0.71	-4.19	1.25	7.81	0.86	4.57	0.67	-2.77	1.10	6.93
Dahra (DAH)	1.03	-1.88	0.58	1.76	0.59	3.21	1.06	-2.03	0.55	1.74	0.59	3.42
Nalohou (NAL)	1.19	6.35	0.68	-8.13	1.80	10.21	1.22	6.44	0.66	-8.39	1.76	10.61
Tondikiboro (TON)	1.07	0.22	0.61	-0.49	1.13	4.03	1.03	0.17	0.61	-0.28	1.07	3.87
Wankama (WAN)	1.11	1.16	0.59	-1.5	1.45	4.41	1.12	1.10	0.59	-1.47	1.43	4.36
All	1.26	0.77	0.73	-2.38	1.33	6.26	1.21	0.86	0.69	-2.09	1.25	6.13

576



577 In order to compare the original SMOS SM with the disaggregated SMOS SM, we filtered the SM  
578 products (original and disaggregated SMOS SM) so that only days included in both time-series were  
579 included in the evaluation (Figure 10). Disaggregated SMOS SM had a slightly lower correlation than  
580 original SMOS SM to *in situ* SM (Figure 10;  $R^2$  in Table 1). However, disaggregated SMOS had a  
581 lower bias, a ratio closer to 1.0, a lower RMSE, and it was slightly closer to the one-to-one ratio (slope  
582 1.21 and 1.26) (Table 1, Figure 10). The largest discrepancy between SMOS SM and the *in situ* SM  
583 was seen for the sites in the southern part of the study area (Belefoungou and Nalohou; Table 1,  
584 Figure 10). These are the sites generating the high SMOS SM in the low *in situ* SM region of Figure  
585 10g. These high SMOS SM values were mainly from the dry season when *in situ* SM was relatively  
586 low (Figure 9b, d).

587 Spatial patterns of disaggregated and original SMOS SM were also evaluated for the entire West  
588 Africa (Figure 11). Major river networks (e.g. Niger, Senegal, Hadejia, etc.) are visible in the  
589 disaggregated product whereas they are not on the original product (Figure 11b). To assess the  
590 potential of the disaggregated SM products for monitoring climate extremes, SM anomalies were  
591 estimated for the period July to September (JAS; growing season months in most of West Africa)  
592 2012 (Figure 11c). Both cases of drought and flooding were observed during that period in West  
593 Africa, and negative SM anomalies are seen in most Senegal and Mali, whereas large patterns of  
594 positive SM anomalies are observed in Central Mali (Figure 11c).

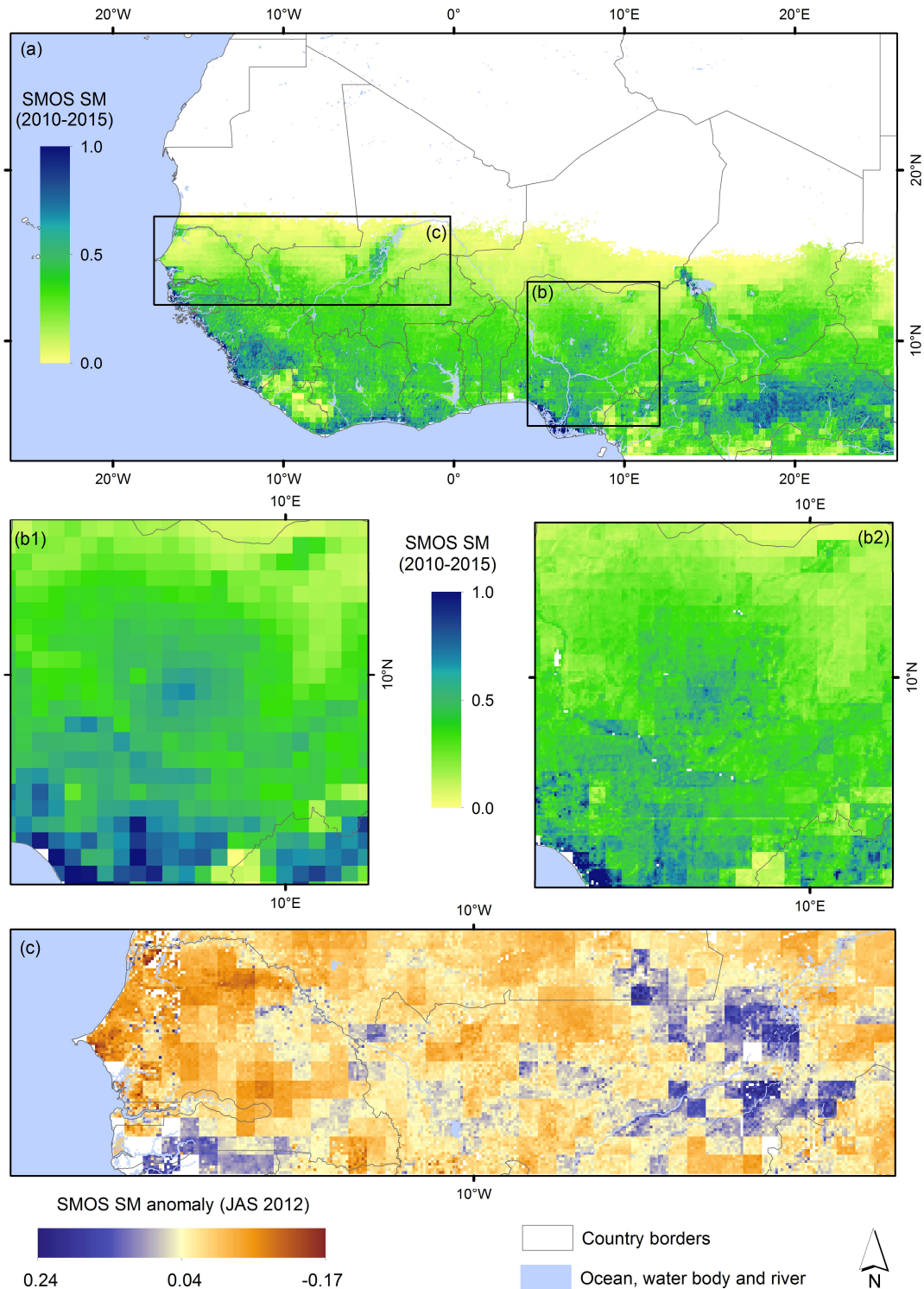


**Figure 11.** SM 2010-2015 average derived from the disaggregated SMOS product over West Africa (a). Main river networks were not visible in the original (non-disaggregated) products (b1), whereas they became apparent after disaggregation (b2). SM extremes (flood and drought) were also captured for the test case of JAS 2012 (c). Filtered and no data are represented in white. The blocky structure observed in the disaggregated products are caused by the original SMOS pixel resolution.

#### 4. Discussion

The use of a higher spatial resolution SM proxy to disaggregate SMOS SM is of high interest as there is a stringent mismatch between the spatial scale at which SM information is provided (e.g.  $\sim 40$  km for SMOS) and the scale of the studied process (Collow et al. 2012). Besides the question of the representability of *in situ* measurements for validating such coarse dataset has often been raised (Dorigo et al. 2015), suggesting that the development of a disaggregated product would grant a more accurate *in situ* validation (Malbêteau et al. 2016). However, if a systematic bias is present in the original SMOS SM (such as seen for the southern sites (Figure 9), seen in the blocky structure of the final disaggregated product (Figure 5e and Figure 11), and as reported by Collow et al. (2012)), the uncertainty will propagate during the disaggregation process, regardless of the quality of the information used for the disaggregation. One large source of uncertainty for SMOS SM is the presence of forest, being the most likely explanation to the systematic bias in the southern sites (Leroux et al. 2013). The disaggregation of SMOS using TVDI as input data improved the relationship for most sites, suggesting that the TVDI spatial heterogeneity is adequately capturing SM heterogeneity within each SMOS pixel.

One of the major challenges here was to produce a time series of TVDI estimates at sub-continental scale in order to best serve the disaggregation process. Commonly TVDI has been used to evaluate SM or evapotranspiration conditions over regions of limited spatial extent (i.e. hydrological basin, sub-national administrative entities, etc.) (de Tomás et al. 2014; Garcia et al. 2014; Stisen et al. 2008). Here TVDI was estimated using a tile approach of 105 by 105 SEVIRI pixels. By fitting TVDI for such tiles the impact of heterogeneous atmospheric and surface condition were alleviated as much as possible and at the same time made TVDI applicable across the subcontinental study area.

It is important to note that TVDI values can only be compared within a given tile (Figure 5d). The exact TVDI value estimated for a certain pixel depends on the location of the wet and dry edge and a specific TVDI value will not represent similar local hydrological conditions when fitted over a tile covering humid tropical forest as over a tile covering semi-arid savanna. Besides, TVDI is not only affected by the exact region used for fitting the triangle, but the size of the tile also has a strong influence (Long et al. 2012). With an increase in tile size more humid and dry conditions are included in the triangular space and the wet and dry edge thereby moves up- and down-wards, respectively, with a strong impact on the TVDI estimates (Figure 7) (Long et al. 2012). Additionally, a small tile size causes large uncertainties in the calculation of the wet and dry edges due to the low number of available pixels (Figure 4) (de Tomás et al. 2014), whereas a large tile size induce uncertainty in relation to heterogeneity of surface roughness and atmospheric forcing (Figure 3). As a compromise we used a relatively large tile size as this was deemed necessary to fulfil the requirements of sufficient amount of data-points for TVDI calculations within parts of the study region (Figure 5c).

It is not only challenging to compare TVDI values originating from different tiles but also values derived at the same location but under different meteorological conditions. Indeed, short-term variability in meteorological parameters (e.g. rainfall, temperature, incoming radiation, wind, cloud cover) is likely to impact the temporal variability in TVDI. If we hypothesize that SM temporal variability can be captured by TVDI time series, rainy season TVDI should be substantially lower than dry season TVDI. As this pattern is not observed (Figure 6), it leads to the questioning of the applicability of TVDI as proxy for monitoring the SM temporal variability. This finding however do not disqualify TVDI as proxy for assessing the spatial variability of SM within a given tile. Here the tile size was set so that a SMOS pixel is never overlapping two different tiles; and each pixel only uses the TVDI heterogeneity within a tile and at a certain point in time for disaggregation of SMOS SM. Future research related to the improvement of the temporal patterns of TVDI could possibly

focus on the use of the newly launched geostationary satellite GOES-R with 1-km spatial resolution which will improve the ability to acquire pure pixels for a comparable smaller area or by using data from constellations of polar orbiting sensors (e.g. MODIS, VIIRS and Sentinel-3) ensuring higher spatial resolution in combination with an adequate temporal resolution.

The TVDI retrievals were found to be very sensitive to errors in the input parameters at the upper range of FVC, challenging the applicability of the TVDI approach for the high FVC regions needed to shape the triangular space. Indeed, it has previously been shown that DisPATCH in the form that it was implemented in this study performs better over semi-arid areas than over temperate zones (Malbêteau et al. 2016). It has also been found that the triangular method underestimates evapotranspiration because the surface temperature of empirically retrieved dry and wet edges are usually under- and overestimated, respectively (Tang and Li 2015). In reality, the evapotranspiration and SM should reach a minimum and maximum level at surface temperatures higher than and lower than what the actual observations show (Tang and Li 2015). This is specifically the case for the upper part of the FVC range (Tang et al. 2010). Incorporating a theoretical dry and wet edge higher and lower than the actual measured level would decrease the sensitivity of the disaggregated product to the input parameters, given that the wet and dry edge would be displaced from the observed values. Tang and Li (2017) developed a physically based model for estimates of endmembers of a trapezoid for evapotranspiration estimates based on both data from earth observation and *in situ* measurements (meteorology, incoming short and longwave radiation, and vegetation height). It is possible that this approach could be adjusted and applied to earth observation and gridded meteorological and vegetation data for estimating endmembers giving such theoretical dry and wet edges. Possibly, this would also result in larger temporal (seasonal) dynamics in TVDI since high FVC observations (i.e. growing season conditions) would be more influenced than low FVC observations (dry season conditions).

Despite these inherent limitations of the TVDI approach, TVDI is found to be a valuable approach for the purpose of disaggregating SM of a SMOS pixel as implemented here. The accuracy of the disaggregated products (RMSE 3.4-10.6 %Vol) were at a similar level as previously published disaggregated SMOS SM products (RMSE varying between 3-11 %Vol) for a range of vegetation types covered here (semi-arid woody savannah, cultivated semi-arid regions, humid woody savannah and tropical forest) (Djamai et al. 2015; Malbêteau et al. 2016; Merlin et al. 2013; Peng et al. 2017; Piles et al. 2016; Piles et al. 2014). Increased details related to major river networks confirms that the disaggregation method driven by the TVDI spatial heterogeneity was successful in improving the spatial representation of the hydrological landscape over West Africa (Figure 11). SM extremes were depicted adequately for the test case of JAS 2012 that coincided with a complex food security crisis in the Sahel. During that year, late, erratic rainfall, together with high food prices and chronic poverty pushed more than 19 million people into food insecurity in the Sahel (de Robert 2012). In August countries already affected by the drought were then hit by heavy rainfall (e.g. in Central Mali, and in several regions in Niger and Nigeria) causing flooding, destroyed infrastructure and damaged crop fields (FEWSNET 2012a, b). Despite the relatively short length of available time series (max. 5 years), seasonal anomalies derived from the disaggregated SM product proved to be an adequate tool to identify both areas affected by extreme high and low SM content. Further investigations should focus on the evaluation of potential monitoring and early warning products at monthly or lower time scale derived from the disaggregated product.

Overall it can be concluded that the disaggregation methodology successfully increased the spatial resolution of SMOS SM and that the disaggregated products can potentially be applied to local SM monitoring for drought/flood risks which is of significant importance for the livelihood of the population in West Africa. Initiatives such as the one set by the European Space Agency (ESA) Data User Element (DUE) GlobTemperature Project that aims at producing and distributing high quality,

consistent LST dataset are of high value for climate and hydrological studies, especially in remote areas with low density *in situ* SM networks. Further research effort should therefore continue the development and distribution of very high temporal time series of LST that are essential for specific activities related to the better understanding of the hydrological cycle, the monitoring, forecasting and early warning of extreme events.

## Acknowledgements

We would like to thank the anonymous reviewers for detailed and constructive comments. FVC were provided by the EUMETSAT Satellite Application Facility on Land Surface Analysis (LSA SAF, <http://landsaf.ipma.pt>). The authors would like to thank Radoslav Guzinski for providing the code for the TVDI computation. This study was funded by the European Space Agency (ESA) Data User Element (DUE) GlobTemperature Project. Torbern Tagesson was additionally funded by the Swedish national Space board (SNSB Dnr 95/16). Stephanie Horion was additionally funded by the Belgian Science Policy office in the frame of the STEREO III U-TURN project. Torbern Tagesson, Stephanie Horion and Rasmus Fensholt were also funded by Danish Council for Independent Research (DFF) Greening of drylands (DFF-6111-00258): Towards understanding ecosystem functioning changes, drivers and impacts on livelihoods..

## References

- Alcaraz-Segura, D., Liras, E., Tabik, S., Paruelo, J., & Cabello, J., 2010. Evaluating the Consistency of the 1982-1999 NDVI Trends in the Iberian Peninsula across Four Time-series Derived from the AVHRR Sensor: LTDR, GIMMS, FASIR, and PAL-II. *Sensors* 10, 1291-1314
- Anderson, M.C., Norman, J.M., Mecikalski, J.R., Otkin, J.A., & Kustas, W.P., 2007. A climatological study of evapotranspiration and moisture stress across the continental United States based on thermal remote sensing: 2. Surface moisture climatology. *J. Geophys. Res. -Atmos.* 112, n/a-n/a

723 Bach, H., & Mauser, W., 1994. Modelling and model verification of the spectral reflectance of soils  
724 under varying moisture conditions, *Proceedings of IGARSS '94 - 1994 IEEE International*  
725 *Geoscience and Remote Sensing Symposium*, Pasadena, CA, USA

726

727 Bonan, G., 2008. *Ecological Climatology: Concepts and Applications*. Cambridge University Press,  
728 New York

729

730 Carlson, T.N., Gillies, R.R., & Schmugge, T.J., 1995. An Interpretation of Methodologies for  
731 Indirect Measurement of Soil-Water Content. *Agric. For. Meteorol.* 77, 191-205

732

733 Carlson, T.N., Perry, E.M., & Schmugge, T.J., 1990. Remote Estimation of Soil-Moisture  
734 Availability and Fractional Vegetation Cover for Agricultural Fields. *Agric. For. Meteorol.* 52, 45-  
735 69

736

737 Collow, T.W., Robock, A., Basara, J.B., & Illston, B.G., 2012. Evaluation of SMOS retrievals of  
738 soil moisture over the central United States with currently available in situ observations. *J.*  
739 *Geophys. Res.-Atmos.* 117

740

741 Crago, R., & Brutsaert, W., 1996. Daytime evaporation and the self-preservation of the evaporative  
742 fraction and the Bowen ratio. *J. Hydrol.* 178, 241-255

743

744 de Beurs, K.M., & Henebry, G.M., 2005. A statistical framework for the analysis of long image  
745 time series. *Int. J. Remote Sens.* 26, 1551-1573

746

747 de Robert, G., 2012. Sahel Food Crisis 2012 - A Cyclical or Exceptional Crisis?, Rome, FAO  
748 report, pp. 6

749

750 de Tomás, A., Nieto, H., Guzinski, R., Salas, J., Sandholt, I., & Berliner, P., 2014. Validation and  
751 scale dependencies of the triangle method for the evaporative fraction estimation over  
752 heterogeneous areas. *Remote Sens. Environ.* 152, 493-511

753

754 Djamai, N., Magagi, R., Goita, K., Merlin, O., Kerr, Y., & Walker, A., 2015. Disaggregation of  
755 SMOS soil moisture over the Canadian Prairies. *Remote Sens. Environ.* 170, 255-268

756

757 Dorigo, W.A., Gruber, A., De Jeu, R.A.M., Wagner, W., Stacke, T., Loew, A., Albergel, C.,  
758 Brocca, L., Chung, D., Parinussa, R.M., & Kidd, R., 2015. Evaluation of the ESA CCI soil moisture  
759 product using ground-based observations. *Remote Sens. Environ.* 162, 380-395

760

761 Eastman, R., Sangermano, F., Ghimire, B., Zhu, H., Chen, H., Neeti, N., Cai, Y., Machado, E.A., &  
762 Crema, S.C., 2009. Seasonal trend analysis of image time series. *Int. J. Remote Sens.* 30, 2721-2726



ECMWF, 2017. ERA5. <https://software.ecmwf.int/wiki/display/CKB/How+to+download+ERA5+data+via+the+ECMWF+Web+API> (accesssed 18-09-2017),

FEWSNET, 2012a. Mali Food Security Outlook update. [www.fews.net/mali](http://www.fews.net/mali) (accesssed 03-05-2017),

FEWSNET, 2012b. West Africa Food Security Outlook Update. <http://www.fews.net/west-africa/food-security-outlook-update/september-2012> (accesssed 03-05-2017),

García-Haro, F.J., Sommer, S., & Kemper, T., 2005. A new tool for variable multiple endmember spectral mixture analysis (VMESMA). *Int. J. Remote Sens.* 26, 2135-2162

Garcia, M., Fernández, N., Villagarcía, L., Domingo, F., Puigdefábregas, J., & Sandholt, I., 2014. Accuracy of the Temperature–Vegetation Dryness Index using MODIS under water-limited vs. energy-limited evapotranspiration conditions. *Remote Sens. Environ.* 149, 100-117

Gillies, R.R., & Carlson, T.N., 1995. Thermal Remote-Sensing of Surface Soil-Water Content with Partial Vegetation Cover for Incorporation into Climate-Models. *J. Appl. Meteorol.* 34, 745-756

GLOBTEMP, 2014. GLOBTEMPERATURE- an ESA DUE initiative. <http://globtemperature.info/> (accesssed 2017-10-16),

Han, Y., Wang, Y.Q., & Zhao, Y.S., 2010. Estimating Soil Moisture Conditions of the Greater Changbai Mountains by Land Surface Temperature and NDVI. *IEEE T. Geosci. Remote Sens.* 48, 2509-2515

Hassan, Q.K., Bourque, C.P.A., Meng, F.R., & Cox, R.M., 2007. A wetness index using terrain-corrected surface temperature and normalized difference vegetation index derived from standard MODIS products: An evaluation of its use in a humid forest-dominated region of eastern Canada. *Sensors* 7, 2028-2048

Hirsch, R.M., & Slack, J.R., 1984. A Nonparametric Trend Test for Seasonal Data with Serial Dependence. *Water Resour. Res.* 20, 727-732

ISMN, 2016. The International Soil Moisture Network. <https://ismn.geo.tuwien.ac.at/> (accesssed 14-02-2016),

- Jiang, Z.Y., Huete, A.R., Didan, K., & Miura, T., 2008. Development of a two-band enhanced vegetation index without a blue band. *Remote Sens. Environ.* 112, 3833-3845
- Jimenez-Munoz, J.C., & Sobrino, J.A., 2008. Split-Window Coefficients for Land Surface Temperature Retrieval From Low-Resolution Thermal Infrared Sensors. *IEEE Geosci. Remote Sens. Lett.* 5, 806-809
- Kerr, Y.H., 2007. Soil moisture from space: Where are we? *Hydrogeol. J.* 15, 117-120
- Kerr, Y.H., Font, J., Martin-Neira, M., & Mecklenburg, S., 2012. Introduction to the Special Issue on the ESA's Soil Moisture and Ocean Salinity Mission (SMOS)-Instrument Performance and First Results. *IEEE T. Geosci. Remote Sens.* 50, 1351-1353
- Kustas, W.P., & Norman, J.M., 1999. Evaluation of soil and vegetation heat flux predictions using a simple two-source model with radiometric temperatures for partial canopy cover. *Agric. For. Meteorol.* 94, 13-29
- Leroux, D.J., Kerr, Y.H., Richaume, P., & Fieuzal, R., 2013. Spatial distribution and possible sources of SMOS errors at the global scale. *Remote Sens. Environ.* 133, 240-250
- Li, H.J., Li, C.Q., Lin, Y., & Lei, Y.P., 2010. Surface temperature correction in TVDI to evaluate soil moisture over a large area. *J. Food Agric. Environ.* 8, 1141-1145
- Li, Z.G., Wang, Y.L., Zhou, Q.B., Wu, J.S., Peng, J., & Chang, H.F., 2008. Spatiotemporal variability of land surface moisture based on vegetation and temperature characteristics in Northern Shaanxi Loess Plateau, China. *J. Arid Environ.* 72, 974-985
- Long, D., Singh, V.P., & Scanlon, B.R., 2012. Deriving theoretical boundaries to address scale dependencies of triangle models for evapotranspiration estimation. *J. Geophys. Res. -Atmos.* 117, D05113
- Louvet, S., Pellarin, T., al Bitar, A., Cappelaere, B., Galle, S., Grippa, M., Gruhier, C., Kerr, Y., Lebel, T., Mialon, A., Mougin, E., Quantin, G., Richaume, P., & de Rosnay, P., 2015. SMOS soil moisture product evaluation over West-Africa from local to regional scale. *Remote Sens. Environ.* 156, 383-394
- Malbêteau, Y., Merlin, O., Molero, B., Rüdiger, C., & Bacon, S., 2016. DisPATCH as a tool to evaluate coarse-scale remotely sensed soil moisture using localized in situ measurements: Application to SMOS and AMSR-E data in Southeastern Australia. *Int. J. Appl. Earth Obs. Geoinf.* 45, 221-234

- Mallick, K., Bhattacharya, B.K., & Patel, N.K., 2009. Estimating volumetric surface moisture content for cropped soils using a soil wetness index based on surface temperature and NDVI. *Agric. For. Meteorol.* 149, 1327-1342
- Merlin, O., Al Bitar, A., Walker, J.P., & Kerr, Y., 2010. An improved algorithm for disaggregating microwave-derived soil moisture based on red, near-infrared and thermal-infrared data. *Remote Sens. Environ.* 114, 2305-2316
- Merlin, O., Escorihuela, M.J., Mayoral, M.A., Hagolle, O., Al Bitar, A., & Kerr, Y., 2013. Self-calibrated evaporation-based disaggregation of SMOS soil moisture: An evaluation study at 3km and 100m resolution in Catalunya, Spain. *Remote Sens. Environ.* 130, 25-38
- Merlin, O., Rudiger, C., Al Bitar, A., Richaume, P., Walker, J.P., & Kerr, Y.H., 2012. Disaggregation of SMOS Soil Moisture in Southeastern Australia. *IEEE T. Geosci. Remote Sens.* 50, 1556-1571
- Minacapilli, M., Iovino, M., & Blanda, F., 2009. High resolution remote estimation of soil surface water content by a thermal inertia approach. *J. Hydrol.* 379, 229-238
- Moran, M.S., Clarke, T.R., Inoue, Y., & Vidal, A., 1994. Estimating Crop Water-Deficit Using the Relation between Surface-Air Temperature and Spectral Vegetation Index. *Remote Sens. Environ.* 49, 246-263
- Moran, M.S., Peters-Lidard, C.D., Watts, J.M., & McElroy, S., 2004. Estimating soil moisture at the watershed scale with satellite-based radar and land surface models. *Can. J. Remote Sens.* 30, 805-826
- Nieto, H., Sandholt, I., Aguado, I., Chuvieco, E., & Stisen, S., 2011. Air temperature estimation with MSG-SEVIRI data: Calibration and validation of the TVX algorithm for the Iberian Peninsula. *Remote Sens. Environ.* 115, 107-116
- Noilhan, J., & Planton, S., 1989. A Simple Parameterization of Land Surface Processes for Meteorological Models. *Monthly Weather Review* 117, 536-549
- Panciera, R., Walker, J.P., Jackson, T.J., Gray, D.A., Tanase, M.A., Ryu, D., Monerris, A., Yardley, H., Rudiger, C., Wu, X.L., Gao, Y., & Hacker, J.M., 2014. The Soil Moisture Active Passive Experiments (SMAPEX): Toward Soil Moisture Retrieval From the SMAP Mission. *IEEE T. Geosci. Remote Sens.* 52, 490-507

882 Patel, N.R., Anapashsha, R., Kumar, S., Saha, S.K., & Dadhwal, V.K., 2009. Assessing potential of  
883 MODIS derived temperature/vegetation condition index (TVDI) to infer soil moisture status. *Int. J.*  
884 *Remote Sens.* 30, 23-39

885  
886 Peng, J., Loew, A., Merlin, O., & Verhoest, N.E.C., 2017. A review of spatial downscaling of  
887 satellite remotely sensed soil moisture. *Reviews of Geophysics* 55, 341-366

888  
889 Piles, M., Petropoulos, G.P., Sánchez, N., González-Zamora, Á., & Ireland, G., 2016. Towards  
890 improved spatio-temporal resolution soil moisture retrievals from the synergy of SMOS and MSG  
891 SEVIRI spaceborne observations. *Remote Sens. Environ.* 180, 403-417

892  
893 Piles, M., Sánchez, N., Vall-llossera, M., Camps, A., Martínez-Fernández, J., Martínez, J., &  
894 González-Gambau, V., 2014. A Downscaling Approach for SMOS Land Observations: Evaluation  
895 of High-Resolution Soil Moisture Maps Over the Iberian Peninsula. *IEEE J. Sel. Top. Appl.* 7,  
896 3845-3857

897  
898 Price, J.C., 1990. Using Spatial Context in Satellite Data to Infer Regional Scale  
899 Evapotranspiration. *IEEE T. Geosci. Remote Sens.* 28, 940-948

900  
901 Proud, S.R., Rasmussen, M.O., Fensholt, R., Sandholt, I., Shisanya, C., Mutero, W., Mbow, C., &  
902 Anyamba, A., 2010. Improving the SMAC atmospheric correction code by analysis of Meteosat  
903 Second Generation NDVI and surface reflectance data. *Remote Sens. Environ.* 114, 1687-1698

904  
905 Proud, S.R., Zhang, Q., Schaaf, C., Fensholt, R., Rasmussen, M.O., Shisanya, C., Mutero, W.,  
906 Mbow, C., Anyamba, A., Pak, E., & Sandholt, I., 2014. The Normalization of Surface Anisotropy  
907 Effects Present in SEVIRI Reflectances by Using the MODIS BRDF Method. *IEEE T. Geosci.*  
908 *Remote Sens.* 52, 6026-6039

909  
910 Rasmussen, M.O., Gottsche, F.M., Olesen, F.S., & Sandholt, I., 2011. Directional Effects on Land  
911 Surface Temperature Estimation From Meteosat Second Generation for Savanna Landscapes. *IEEE*  
912 *T. Geosci. Remote Sens.* 49, 4458-4468

913  
914 Sadeghi, M., Jones, S.B., & Philpot, W.D., 2015. A linear physically-based model for remote  
915 sensing of soil moisture using short wave infrared bands. *Remote Sens. Environ.* 164, 66-76

916  
917 Sandholt, I., Rasmussen, K., & Andersen, J., 2002. A simple interpretation of the surface  
918 temperature/vegetation index space for assessment of surface moisture status. *Remote Sens.*  
919 *Environ.* 79, 213-224

920  
921 Schmugge, T., 1978. Remote-Sensing of Surface Soil-Moisture. *J. Appl. Meteorol.* 17, 1549-1557

922  
923 Sobrino, J.A., & Romaguera, M., 2004. Land surface temperature retrieval from MSG1-SEVIRI  
924 data. *Remote Sens. Environ.* 92, 247-254

925  
926 Stisen, S., Sandholt, I., Norgaard, A., Fensholt, R., & Jensen, K.H., 2008. Combining the triangle  
927 method with thermal inertia to estimate regional evapotranspiration - Applied to MSG-SEVIRI data  
928 in the Senegal River basin. *Remote Sens. Environ.* 112, 1242-1255

929  
930 Stisen, S., Sandholt, I., Nørgaard, A., Fensholt, R., & Eklundh, L., 2007. Estimation of diurnal air  
931 temperature using MSG SEVIRI data in West Africa. *Remote Sens. Environ.* 110, 262-274

932  
933 Sun, L., Sun, R., Li, X.W., Liang, S.L., & Zhang, R.H., 2012. Monitoring surface soil moisture  
934 status based on remotely sensed surface temperature and vegetation index information. *Agric. For.*  
935 *Meteorol.* 166, 175-187

936  
937 Tagesson, T., Fensholt, R., Cappelaere, B., Mougin, E., Horion, S., Kergoat, L., Nieto, H.,  
938 Ehammer, A., Demarty, J., & Ardö, J., 2016. Spatiotemporal variability in carbon exchange fluxes  
939 across the Sahel *Agric. For. Meteorol.* 226–227, 108-118

940  
941 Tagesson, T., Fensholt, R., Guiro, I., Rasmussen, M.O., Huber, S., Mbow, C., Garcia, M., Horion,  
942 S., Sandholt, I., Rasmussen, B.H., Göttsche, F.M., Ridler, M.-E., Olén, N., Olsen, J.L., Ehammer,  
943 A., Madsen, M., Olesen, F.S., & Ardö, J., 2015. Ecosystem properties of semi-arid savanna  
944 grassland in West Africa and its relationship to environmental variability. *Global Change Biol.* 21,  
945 250-264

946  
947 Tang, R., & Li, Z.-L., 2015. Evaluation of two end-member-based models for regional land surface  
948 evapotranspiration estimation from MODIS data. *Agric. For. Meteorol.* 202, 69-82

949  
950 Tang, R., & Li, Z.L., 2017. An End-Member-Based Two-Source Approach for Estimating Land  
951 Surface Evapotranspiration From Remote Sensing Data. *IEEE T. Geosci. Remote Sens. PP*, 1-15

952  
953 Tang, R.L., Li, Z.L., & Tang, B.H., 2010. An application of the T-s-VI triangle method with  
954 enhanced edges determination for evapotranspiration estimation from MODIS data in and and semi-  
955 arid regions: Implementation and validation. *Remote Sens. Environ.* 114, 540-551

956  
957 Trigo, I.F., Dacamara, C.C., Viterbo, P., Roujean, J.-L., Olesen, F., Barroso, C., Camacho-de-Coca,  
958 F., Carrer, D., Freitas, S.C., García-Haro, J., Geiger, B., Gellens-Meulenberghs, F., Ghilain, N.,  
959 Meliá, J., Pessanha, L., Siljamo, N., & Arboleda, A., 2011. The Satellite Application Facility for  
960 Land Surface Analysis. *Int. J. Remote Sens.* 32, 2725-2744

961

- 962 Trigo, I.F., Peres, L.F., DaCamara, C.C., & Freitas, S.C., 2008. Thermal Land Surface Emissivity  
963 Retrieved From SEVIRI/Meteosat. *IEEE T. Geosci. Remote Sens.* 46, 307-315
- 964
- 965 Vanbelle, G., & Hughes, J.P., 1984. Nonparametric-Tests for Trend in Water-Quality. *Water*  
966 *Resour. Res.* 20, 127-136
- 967
- 968 Vinukollu, R.K., Wood, E.F., Ferguson, C.R., & Fisher, J.B., 2011. Global estimates of  
969 evapotranspiration for climate studies using multi-sensor remote sensing data: Evaluation of three  
970 process-based approaches. *Remote Sens. Environ.* 115, 801-823
- 971
- 972 Wan, Z.M., & Dozier, J., 1996. A generalized split-window algorithm for retrieving land-surface  
973 temperature from space. *IEEE T. Geosci. Remote Sens.* 34, 892-905
- 974
- 975 Wang, C.Y., Qi, S.H., Niu, Z., & Wang, J.B., 2004. Evaluating soil moisture status in China using  
976 the temperature-vegetation dryness index (TVDI). *Can. J. Remote Sens.* 30, 671-679
- 977
- 978 Wang, J., Ling, Z., Wang, Y., & Zeng, H., 2016. Improving spatial representation of soil moisture  
979 by integration of microwave observations and the temperature–vegetation–drought index derived  
980 from MODIS products. *ISPRS Journal of Photogrammetry and Remote Sensing* 113, 144-154
- 981
- 982 Wang, K.C., Li, Z.Q., & Cribb, M., 2006. Estimation of evaporative fraction from a combination of  
983 day and night land surface temperatures and NDVI: A new method to determine the Priestley-  
984 Taylor parameter. *Remote Sens. Environ.* 102, 293-305
- 985
- 986 Wigneron, J.P., Kerr, Y., Waldteufel, P., Saleh, K., Escorihuela, M.J., Richaume, P., Ferrazzoli, P.,  
987 de Rosnay, P., Gurney, R., Calvet, J.C., Grant, J.P., Guglielmetti, M., Hornbuckle, B., Mätzler, C.,  
988 Pellarin, T., & Schwank, M., 2007. L-band Microwave Emission of the Biosphere (L-MEB) Model:  
989 Description and calibration against experimental data sets over crop fields. *Remote Sens. Environ.*  
990 107, 639-655

991

## 992 **Appendix A. Mathematical derivations of Equation 5 and 7**

993 **Equation 5 was derived from equation 4:**

$$994 \quad SEE_{\text{model}} = \frac{1}{2} - \frac{1}{2} \cos \left( \pi \times \frac{SM}{SM_p} \right) \quad (4)$$

995 Multiply both sides with -2:

$$-2\text{SEE}_{\text{model}} = -1 + \cos\left(\pi \times \frac{\text{SM}}{\text{SM}_p}\right)$$

Add 1 to both sides:

$$1 - 2\text{SEE}_{\text{model}} = \cos\left(\pi \times \frac{\text{SM}}{\text{SM}_p}\right)$$

Multiply both sides with arccos:

$$\arccos(1 - 2\text{SEE}_{\text{model}}) = \pi \times \frac{\text{SM}}{\text{SM}_p}$$

Put  $\text{SM}_p$  on the left side and put  $\arccos(1 - 2\text{SEE}_{\text{model}})$  in the denominator on the right side and equation 5 is derived:

$$\text{SM}_p = \frac{\pi \times \text{SM}_{\text{SMOS}}}{\arccos(1 - 2\langle \text{SEE}_{\text{SEVIRI}} \rangle_{\text{SMOS}})} \quad (5)$$

**Equation 7 was derived by taking the derivative of equation 6:**

$$\text{SM}_{\text{model}} = \frac{\text{SM}_p}{\pi} \arccos(1 - 2\text{SEE}) \quad (6)$$

The derivative of  $\arccos(x)$  is:

$$\frac{\partial \arccos(x)}{\partial x} = -\frac{1}{\sqrt{1-x^2}}$$

Then, by setting  $x=(1-2\text{SEE})$  and taking the derivative of  $x$  we get:

$$\frac{\partial \text{SM}_{\text{model}}}{\partial x} = -\frac{\frac{\text{SM}_p}{\pi}}{\sqrt{1-x^2}}$$

Then by taking the derivative of SEE on  $x$  we get:

$$1012 \quad \frac{\partial x}{\partial \text{SEE}} = -2$$

1013 Then by multiplying both sides with the derivative of SEE on x we get:

$$1014 \quad \frac{\partial \text{SM}_{\text{model}}}{\partial x} \times \frac{\partial x}{\partial \text{SEE}} = -\frac{\frac{\text{SM}_p}{\pi}}{\sqrt{1-x^2}} \times -2 \Rightarrow \frac{\partial \text{SM}_{\text{model}}}{\partial \text{SEE}} = \frac{2\left(\frac{\text{SM}_p}{\pi}\right)}{\sqrt{1-x^2}}$$

1015 Finally, by setting  $x = (1-2\text{SEE})$  equation 7 is derived:

$$1016 \quad \frac{\partial \text{SM}_{\text{model}}}{\partial \text{SEE}} = \frac{2\left(\frac{\text{SM}_p}{\pi}\right)}{\sqrt{1-(1-2\text{SEE})^2}}$$

1017

## 1018 **Appendix B. Mathematical derivations indicating that TVDI is a proxy of SEE**

1019 According Merlin et al. (2012) SEE can be calculated as:

$$1020 \quad \text{SEE} = \frac{T_{\text{soil\_max}} - T_{\text{soil}}}{T_{\text{soil\_max}} - T_{\text{soil\_min}}} \quad (\text{B1})$$

1021 where  $T_{\text{soil}}$  is the soil temperature;  $T_{\text{soil\_min}}$  is minimum  $T_{\text{soil}}$ ; and  $T_{\text{soil\_max}}$  is maximum  $T_{\text{soil}}$ .

1022 Soil temperature and  $T_{\text{soil\_max}}$  can be calculated as (Merlin et al. 2010; Merlin et al. 2012):

$$1023 \quad T_{\text{soil}} = \frac{\text{LST} - (\text{FVC} \times T_{\text{vegetation}})}{1 - (\text{FVC} \times T_{\text{vegetation}})}$$

$$1024 \quad T_{\text{soil\_max}} = \frac{\text{LST}_{\text{max}} - (\text{FVC} \times T_{\text{vegetation}})}{1 - (\text{FVC} \times T_{\text{vegetation}})}$$

1025 If we put these two into equation B1; we get:

$$1026 \quad \text{SEE} = \frac{\frac{\text{LST}_{\text{max}} - (\text{FVC} \times T_{\text{vegetation}})}{(1 - \text{FVC})} - \frac{\text{LST} - (\text{FVC} \times T_{\text{vegetation}})}{(1 - \text{FVC})}}{\frac{\text{LST}_{\text{max}} - (\text{FVC} \times T_{\text{vegetation}})}{(1 - \text{FVC})} - T_{\text{soil\_min}}} \Rightarrow$$

$$1027 \quad \text{SEE} = \frac{\frac{\text{LST}_{\text{max}} - (\text{FVC} \times T_{\text{vegetation}})}{(1 - \text{FVC})} - \frac{\text{LST} - (\text{FVC} \times T_{\text{vegetation}})}{(1 - \text{FVC})}}{\frac{\text{LST}_{\text{max}} - (\text{FVC} \times T_{\text{vegetation}})}{(1 - \text{FVC})} - \frac{T_{\text{soil\_min}}(1 - \text{FVC})}{(1 - \text{FVC})}} \Rightarrow$$

$$1028 \quad \text{SEE} = \frac{\text{LST}_{\text{max}} - (\text{FVC} \times T_{\text{vegetation}}) - \text{LST} + (\text{FVC} \times T_{\text{vegetation}})}{\text{LST}_{\text{max}} - (\text{FVC} \times T_{\text{vegetation}}) - T_{\text{soil\_min}}(1 - \text{FVC})} \Rightarrow$$



$$1029 \quad SEE = \frac{LST_{\max} - LST}{LST_{\max} - (FVC \times T_{\text{vegetation}}) - T_{\text{soil\_min}}(1 - FVC)} \Rightarrow$$

$$1030 \quad SEE = \frac{LST_{\max} - LST}{LST_{\max} - (FVC \times T_{\text{vegetation}}) - T_{\text{soil\_min}} + (FVC \times T_{\text{soil\_min}})}$$

1031 Given that vegetation temperature ( $T_{\text{vegetation}}$ ) is approximately the same as minimum soil  
 1032 temperature ( $T_{\text{soil\_min}}$ ) (Merlin et al. 2010), and that  $T_{\text{soil\_min}}$  can be estimated as minimum LST within  
 1033 a window tile (the wet edge) (Merlin et al. 2010) this leads us to:

1034

$$1035 \quad SEE \approx \frac{LST_{\max} - LST}{LST_{\max} - T_{\text{soil\_min}}} \approx \frac{LST_{\max} - LST}{LST_{\max} - LST_{\min}} = (1 - TVDI)$$

1036

## Figure Captions

**Figure 1.** Conceptual triangle space with the land surface temperature (LST) or morning rise temperature (dTS) on the y-axis and Fraction of Vegetation Cover (FVC) on the x-axis. The blue line is the wet edge (TVDI=0.00) and the red line is the dry edge (TVDI=1.00). The grey dotted lines are TVDI examples of 0.25, 0.50, and 0.75. The figure is adapted from Peng et al. (2017).

**Figure 2.** Study area with the location of the *in situ* validation sites. The averaged fraction of vegetation cover (FVC) for year 2011 is used as background to illustrate the important north-south gradient in vegetation cover.

**Figure 3.** Dynamic range in surface properties and atmospheric forcing influencing the homogeneity of available energy within the triangular space. Influence of tile size (y-axis) on the percentiles of the time series (x-axis) of the dynamic range in daily averaged a) forecast surface roughness (FSR) (m); b), surface solar radiation downwards (SSRD) ( $\text{W m}^{-2}$ ); c) total column water vapour (TCWV) ( $\text{kg m}^{-2}$ ); d) wind speed at 100 m height (WS) ( $\text{m s}^{-1}$ ); and e) air temperature at the 975 hPa level ( $T_{\text{air}}$ ) (K) for 1) the Dahra and 2) the Nalohou field sites. The percentiles on the x-axis gives an indication of the fraction of the time series for a given tile size having a dynamic range smaller than the value shown by the colour. For the z-axis, dark blue indicates high homogeneity (i.e. small dynamic range) in surface properties or atmospheric forcing, whereas yellow indicates low homogeneity.

**Figure 4.** Influence of tile size (y-axis) on the percentiles of the time series (x-axis) of the parameters influencing the triangular shape. a) Number of points including in the triangle (N); b) range in fraction of vegetation cover (FVC); and c) correlation coefficient of the dry edge slope (r) for 1) the Dahra and, 2) the Nalohou field sites. The percentiles on the x-axis gives an indication of the fraction of the time-series for a given tile size having a range smaller than the value shown by the colour.

**Figure 5.** (a) Fraction of data coverage for the input data (dTS and FVC) used in the TVDI calculations; (b) fraction of data coverage for the TVDI calculations when TVDI was filtered based on both TVDI tile statistics and quality flags in input data. (c) Average data exclusion fraction depending on latitude; blue is the fraction of rejected input data, red is the fraction rejected in relation to the TVDI calculation, and black is the total rejected fraction. Included are also: (d) average TVDI for the entire study period; and (e) disaggregated SMOS SM averaged for the entire study period.

**Figure 6.** Time series of the input parameters, extracts from the TVDI calculation tiles, and final TVDI estimates for (1) Dahra and (2) Nalohou: (a.) fraction of vegetation cover (FVC); (b) unfiltered (red) and filtered (black) morning rise temperature (dTS); (c) range of FVC in the TVDI tiles; (d)

total number of points included in the triangle (N); (e) coefficient of determination ( $R^2$ ) for the dry edge fit; (f) wet edge; and (g) dry edge slope. Included are also (h) filtered (black) and gap-filled (red) TVDI estimates (black).

**Figure 7.** Sensitivity of TVDI to input data and equation parameters: a) morning rise temperature (dTS; °C); b) fraction of vegetation cover (FVC); c) dry edge intercept (DI); d) dry edge slope (DS); and e) wet edge (W). The % for the temperatures (dTS, DI, and W) and the FVC is a % change in relation to the range of the triangle. During the analysis we changed one parameter at the time and the rest remained stable.

**Figure 8.** Sensitivity of disaggregated SMOS soil moisture (SM; %Vol) to changes in TVDI. Average TVDI in equation 8 was set to a) 0.25, b) 0.50 and c) 0.75. First row (1) shows the actual disaggregated SM for each original SMOS SM -TVDI case and second row (2) shows the changes in disaggregated SM for each 0.01 error in TVDI for each SM -TVDI case.

**Figure 9.** Time series of *in situ* measured soil moisture (SM (%Vol)) (thin black line) and Soil moisture and Ocean Salinity (SMOS) SM (grey dots) for: a) Banizoumbou; b) Belefoungou; c) Dahra; d) Nalohou e) Tondikiboro; and f) Wankama. The location of the different sites is shown in Figure 2.

**Figure 10.** Relationship between *in situ* and both original (1) and disaggregated (2) Soil Moisture and Ocean Salinity (SMOS) soil moisture (SM; %Vol) for the pixels used in the evaluation of the disaggregation methodology. The subplots are: a) Banizoumbou; b) Belefoungou; c) Dahra; d) Nalohou; e) Tondikiboro; f) Wankama; and g) all sites combined. The grey line is the ordinary least square linear regression and the black line is the one-to-one ratio. Statistics of the slopes are given in Table 1. The location of the sites can be seen in figure 2.

**Figure 11.** SM 2010-2015 average derived from the disaggregated SMOS product over West Africa (a). Main river networks were not visible in the original (non-disaggregated) products (b1), whereas they became apparent after disaggregation (b2). SM extremes (flood and drought) were also captured for the test case of JAS 2012 (c). Filtered and no data are represented in white. The blocky structure observed in the disaggregated products are caused by the original SMOS pixel resolution.